NAVAL POSTGRADUATE SCHOOL
Monterey, California

THESIS

FACTORS AFFECTING THE STRENGTH AND TOUGHNESS OF ULTRA-LOW CARBON STEEL WELD METAL

by

Jonathon J. Van Slyke

December 1999

Thesis Advisor: Alan G. Fox

REPORT DOCUMENTATION PAGE

Form Approved
OMB No. 0704-0188

1. AGENCY USE ONLY *(Leave blank)*	2. REPORT DATE December 1999	3. REPORT TYPE AND DATES COVERED Engineer's Thesis

4. TITLE AND SUBTITLE:
FACTORS AFFECTING THE STRENGTH AND TOUGHNESS OF ULTRA-LOW CARBON STEEL WELD METAL

5. FUNDING NUMBERS

6. AUTHOR(S) **Van Slyke, Jonathon J.**

7. PERFORMING ORGANIZATION NAME(S) AND ADDRESS(ES)
Naval Postgraduate School
Monterey, CA 93943-5000

8. PERFORMING ORGANIZATION REPORT NUMBER

9. SPONSORING / MONITORING AGENCY NAME(S) AND ADDRESS(ES)
Naval Surface Warfare Center, Carderock Division, 9500 McArthur Boulevard, Bethesda, Maryland 20084-5000

10. SPONSORING/MONITORING AGENCY REPORT NUMBER

11. SUPPLEMENTARY NOTES
The views expressed here are those of the author and do not reflect the official policy or position of the Department of Defense or the U.S. Government.

12a. DISTRIBUTION / AVAILABILITY STATEMENT
Approved for public release; distribution is unlimited.

12b. DISTRIBUTION CODE

13. ABSTRACT The factors that affect strength and toughness of ten ultra-low carbon steel weld samples (HSLA-80 and HSLA-100), welded using the gas metal arc welding (GMAW) process and new ultra-low carbon consumable electrodes, were studied. The analysis was confined only to the weld metal, and the base metal was not considered. Analysis methods included optical microscopy, scanning electron microscopy, and transmission electron microscopy. Energy dispersive x-ray analysis was performed in the transmission electron microscope to analyze the chemical composition of non-metallic inclusions.

The microstructure was found to be primarily granular ferrite with some primary ferrite, bainite, and martensite. Very little acicular ferrite was found (< 18 %). Because of this, to get the best mechanical properties in the weld, the size and volume fraction of non-metallic inclusions needs to be minimized. This can be accomplished by minimizing the amount of oxygen while increasing the amount of titanium and aluminum in the weld metal.

EDX analysis revealed that the non-metallic inclusions were multi-phase particles with two predominant phases: a TiO-MnO phase and a $MnO\text{-}SiO_2\text{-}Al_2O_3$ phase. Copper-sulfide caps were also found on the surface of some inclusions. This inclusion chemistry is typical of what is found in welding HSLA steel.

14. SUBJECT TERMS
HSLA-80, HSLA-100, Gas Metal Arc Welding, Ultra-Low Carbon Steel, Non-Metallic Inclusions

15. NUMBER OF PAGES
95

16. PRICE CODE

17.SECURITY CLASSIFICATION OF REPORT	18.SECURITYCLASSIFICATION OF THIS PAGE	19. SECURITY CLASSIFICATION OF ABSTRACT	20. LIMITATION OF ABSTRACT
Unclassified	Unclassified	Unclassified	UL

NSN 7540-01-280-5500

Standard Form 298 (Rev. 2-89)
Prescribed by ANSI Std. 239-18 298-102

Approved for public release; distribution is unlimited.

FACTORS AFFECTING THE STRENGTH AND TOUGHNESS OF ULTRA-LOW CARBON STEEL WELD METAL

Jonathon J. Van Slyke
Lieutenant, United States Navy
B. S., University of Idaho, 1993

Submitted in partial fulfillment of the
requirements for the degree of

MECHANICAL ENGINEER

from the

NAVAL POSTGRADUATE SCHOOL
December 1999

ABSTRACT

The factors that affect strength and toughness of ten ultra-low carbon steel weld samples (HSLA-80 and HSLA-100), welded using the gas metal arc welding (GMAW) process and new ultra-low carbon consumable electrodes, were studied. The analysis was confined only to the weld metal, and the base metal was not considered. Analysis methods included optical microscopy, scanning electron microscopy, and transmission electron microscopy. Energy dispersive x-ray analysis was performed in the transmission electron microscope to analyze the chemical composition of non-metallic inclusions.

The microstructure was found to be primarily granular ferrite with some primary ferrite, bainite, and martensite. Very little acicular ferrite was found (< 18 %). Because of this, to get the best mechanical properties in the weld, the size and volume fraction of non-metallic inclusions needs to be minimized. This can be accomplished by minimizing the amount of oxygen while increasing the amount of titanium and aluminum in the weld metal.

EDX analysis revealed that the non-metallic inclusions were multi-phase particles with two predominant phases: a TiO-MnO phase and a $MnO\text{-}SiO_2\text{-}Al_2O_3$ phase. Copper-sulfide caps were also found on the surface of some inclusions. This inclusion chemistry is typical of what is found in welding HSLA steel.

TABLE OF CONTENTS

ACKNOWLEDGEMENT

I would like to thank Dr. Alan G. Fox for his enthusiasm, guidance and support throughout the creation of this thesis.

I would also like to thank Dr. Sarath Menon and Dr. Nagarajan Rajagopalan for their time, knowledge, guidance, and patience as they assisted me in completing the experimental stage of this thesis.

I owe the deepest debt of gratitude to my wife, Mary, and my children, Christian and Cera, for their love and support, and for keeping me sane during this time.

Finally, I cannot express the debt that I owe to God for setting the events in motion that led to the creation of this thesis and for his love, guidance and support.

I. INTRODUCTION

High strength steels are the primary structural materials used in building naval ships and submarines. HY-80 and HY-100 steel plates (0.13-0.17 wt% carbon) are welded together to make up the hulls of these vessels. The main difficulties with using these steels are the strict pre-heat and inter-pass temperature controls required to prevent hydrogen induced cracking in the weld. [Ref. 1, 4] High strength low alloy (HSLA) steels (~0.05 wt% carbon) have recently been developed to reduce the risks of hydrogen induced cracking and therefore relax the restrictions for pre-heat and inter-pass temperature control.

Figure 1-1 shows the Graville Diagram [Ref. 2], which graphically predicts the "weldability" of a steel based on its carbon content and equivalent carbon content (a measure of the hydrogen-cracking sensitivity of a weld [Ref. 1,2]). This figure shows that HY-80 and HY-100 both fall into zone III (difficult to weld) but HSLA-80 and HSLA-100 both fall into zone I (easy to weld) because of their lower carbon contents.

In order to take advantage of the weldability of HSLA steels, suitable consumable electrodes are required. Until now, the same consumables that have been used to weld HY steels are used to weld HSLA steels. This process still requires preheat and interpass temperature controls to prevent cracking. The National Center for Excellence in Metalworking Technology (NCEMT) is currently working with Naval Sea Systems Command to develop and verify advanced welding consumables for use in welding

HSLA steels without preheat or interpass temperature controls, and for welding HY steels with appropriate temperature controls in effect.

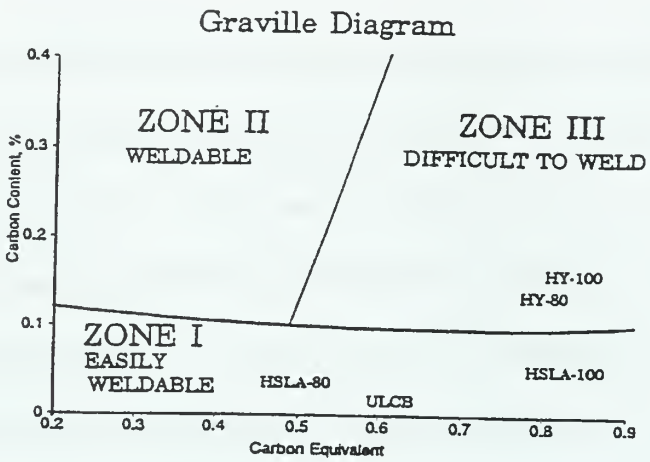

$$C.E. = C + \frac{Mn + Si}{6} + \frac{Ni + Cu}{15} + \frac{Cr + Mo + V}{5}$$

Figure 1-1: Graville Diagram (Graville, 1978)

The present study continues to investigate the fundamental characteristics of welds produced by gas metal arc welding of HSLA steels. This study is limited only to the weld metal and does not include the heat-affected zone of the base metal. The goal is to understand how the weld characteristics affect the microstructure, and how the microstructure affects the strength and toughness of the weld. Ten samples were produced by NSWC. Of these samples, one contained the entire weld region and some of the base metal and the rest were sections of tensile test specimen. The samples had varying composition, thickness, and cooling rate. The welds were performed using ultra-low carbon consumables (ARC100N and ARC100R). These samples were analyzed to determine their microstructure, and non-metallic inclusion size, volume fraction and chemistry. Appendix A shows the characteristics of the weld samples.

II. BACKGROUND

A. HIGH STRENGTH LOW ALLOY STEELS

High yield strength steels like HY-80 and HY-100 are quenched and tempered steels that obtain most of their strength from solid solution strengthening using carbon as the solute (0.12-0.18 wt% [Ref. 3]). High carbon content is deleterious to the toughness of the steel since it promotes the formation of a brittle, high carbon martensite phase upon rapid cooling from the austenite region (as typically associated with welding). This brittle martensite cracks due to thermal stresses, stresses due to constraints, and the presence of hydrogen. Current preventative measures include control of preparation, storage, and issue of electrodes; preheat and interpass temperatures; heat input; welding sequence; weather protection; nondestructive testing; training and qualification of welders; and avoidance of highly constrained welds by design. [Ref. 4]

High strength low alloy steels (HSLA) were developed by the Navy to reduce the limitations on welding (preheat and inter-pass temperature control) and therefore the cost of welding. HSLA steels have potentially the same or better strength and toughness properties as the HY steels, but their reduced carbon content makes them inherently more weldable. The first HSLA steel used in fleet construction was HSLA-80. It is derived from ASTM-710 grade steel and is a polygonal/acicular ferritic alloy employing microalloying and precipitation strengthening. Its low carbon content (0.04-0.08wt%) results in good weldability. [Ref. 4]

HSLA-100 steel was initially developed for applications in submarine non-pressure hull structures. It was developed using a fundamental alloy design program, taking advantage of fracture process modeling to reduce the ductile-to-brittle transition temperature. It also relies on microalloying for solid solution strengthening and on copper precipitation strengthening. [Ref. 4]

HSLA-80 and HSLA-100 rely on manganese, niobium, nickel, and copper for strength. Manganese is the best alternative to carbon for improving strength without compromising toughness. Balanced additions of manganese have been found to improve toughness because of increased proportions of acicular ferrite in combination with a general refinement of the microstructure. Niobium is added to form Nb(CN) precipitates, which pin prior austenite grain boundaries, which keeps the microstructure fine. However, excess precipitation of Nb(CN) in the ferrite can cause a deterioration in toughness. Nickel is added as a solid solution strengthening agent while copper is added as a precipitation strengthener. Manganese, nickel, and copper also act as austenite stabilizers. [Ref. 5]

Other elements such as aluminum and titanium, that are present in trace amounts in the base metal and filler wire, promote the formation of acicular ferrite in the weld metal. They are strong oxidizers, which form non-metallic inclusions that are favorable nucleation sites for acicular ferrite, and reduce the soluble oxygen content in the weld. Boron, which may also be present, segregates to austenite grain boundaries where it lowers the grain boundary energy suppressing the formation of primary ferrite. This can be represented on a continuous cooling transformation diagram (CCTD) as a shifting of the primary ferrite curve to the right, and increasing the region over which acicular and

granular ferrite would form (Figure 2-3). Primary ferrite and the CCTD will be discussed in more detail later. Excess titanium is also helpful in scavenging free nitrogen in the weld, which would form boron-nitride, which does not suppress the formation of proeutectoid ferrite. Excess aluminum (>0.025 wt%), on the other hand, has been seen to interfere with acicular ferrite formation. [Ref. 5]

B. GAS METAL ARC WELDING

Gas metal are welding (GMAW) is the most common method of welding used in construction and repair of naval ships and submarines. It has deeper penetration, and a higher deposition rate than gas tungsten arc welding (GTAW), and therefore requires fewer passes and less time, which translates to lower cost. Submerged arc welding (SAW) results in deeper penetration and a higher deposition rate than GMAW, but is limited in applications due to gravitational effects on the granular flux, while GMAW can be used in virtually all positions and orientations. [Ref. 1]

"Gas metal arc welding (GMAW) is an electric arc welding process that produces coalescence of metals by heating them with an arc established between a continuous filler metal (consumable) electrode and the work piece." [Ref. 1] GMAW uses a continuous wire feed process where the wire acts as a consumable electrode. A cover gas is blown around the arc and weld pool to protect the molten metal from the atmosphere. Additional protection from the atmosphere can be attained using filler wires that contain a flux core. The flux assists the cover gas in protecting the molten metal from the

atmosphere. The flux also provides deoxidizers to cleanse the weld metal, provides ionizing compounds that stabilize the arc, and provides a means of adding alloying elements and/or metal powders (alloying elements control the composition while metal powders increase the deposition rate). Figure 2-1 shows a sketch of the GMAW process while Figure 2-2 shows a typical multipass GMAW weld cross section.

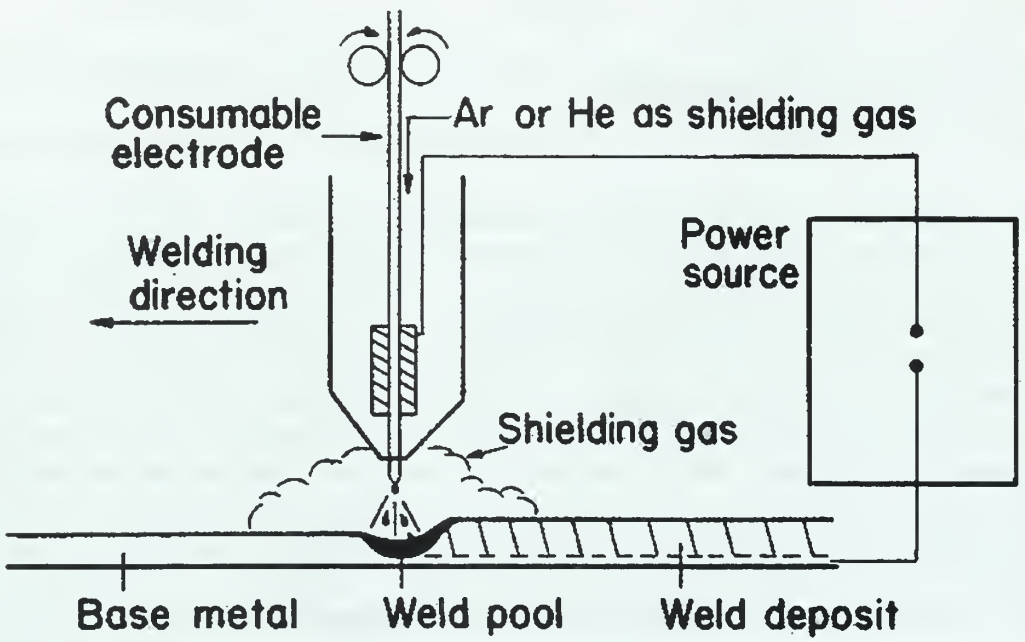

Figure 2-1: Sketch of the gas metal arc welding process.

The stability of the arc in GMAW is greatly affected by the shape of the electrode tip and the arc length. Since the electrode is consumable, the electrode tip and arc length cannot be optimally maintained. Therefore, a cover gas of 95% Ar and 5% CO_2 (C5) is used by the Navy for welding high strength steels instead of 100% Argon. The CO_2 acts as an arc-stabilizer, but it also results in increased oxygen and carbon contents in the weld metal. [Ref. 6] The affect of weld metal oxygen content will be discussed later, along with deoxidation.

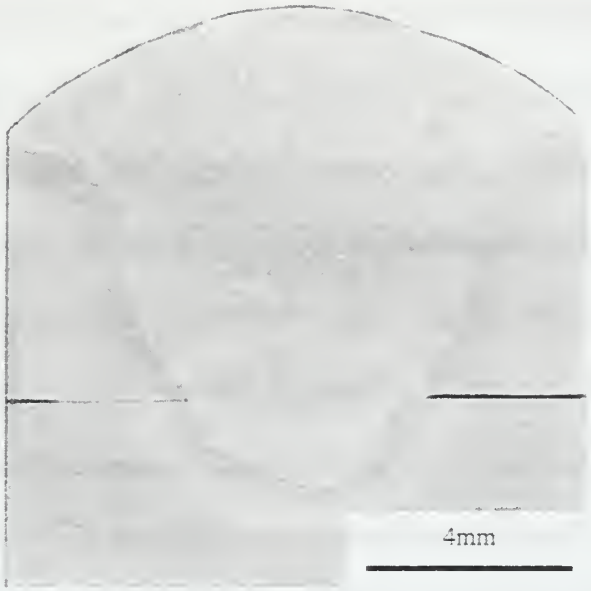

Figure 2-2: Multipass gas metal arc weld in HSLA-80 steel (PD 21150)

There are three types of GMAW processes. These are identified by the method of metal transfer used, which can be short-circuiting, globular, or spray. Short-circuiting results from physical contact between the filler wire and the weld pool, which results in a continuous transfer of metal from the electrode to the weld pool. Globular and spray transfer both result in discrete amounts of the filler wire being transferred across the arc to the weld pool. The welding current, electrode size, and shielding gas are the major factors affecting the type of metal transfer. [Ref 1, 6]

Direct-current reverse polarity (DCRP) is the most used configuration for GMAW because it results in a stable arc, smooth metal transfer, low spatter loss, and good weld penetration. This configuration is used with the spray transfer method in steel applications. Direct-current straight polarity (DCSP) and alternating current have difficulty in maintaining smooth metal transfer and are seldom used, except that DCSP is used in conjunction with globular metal transfer in some aluminum applications. [Ref. 1]

C. WELD MICROSTRUCTURE

The international Welding Society established the classifications of steel weld metal microstructures described below. [Ref. 8] Figure 2-3 shows a representative continuous cooling transformation diagram for HSLA steel, which shows the relative cooling rates and transformation temperatures of each of the microstructures. [Ref. 9] The final weld metal microstructure depends on complex interactions between the total alloying content; the concentration, chemical composition, and size distribution of non-metallic inclusions; the solidification microstructure, the prior austenite grain size, and the weld thermal cycle. [Ref. 5]

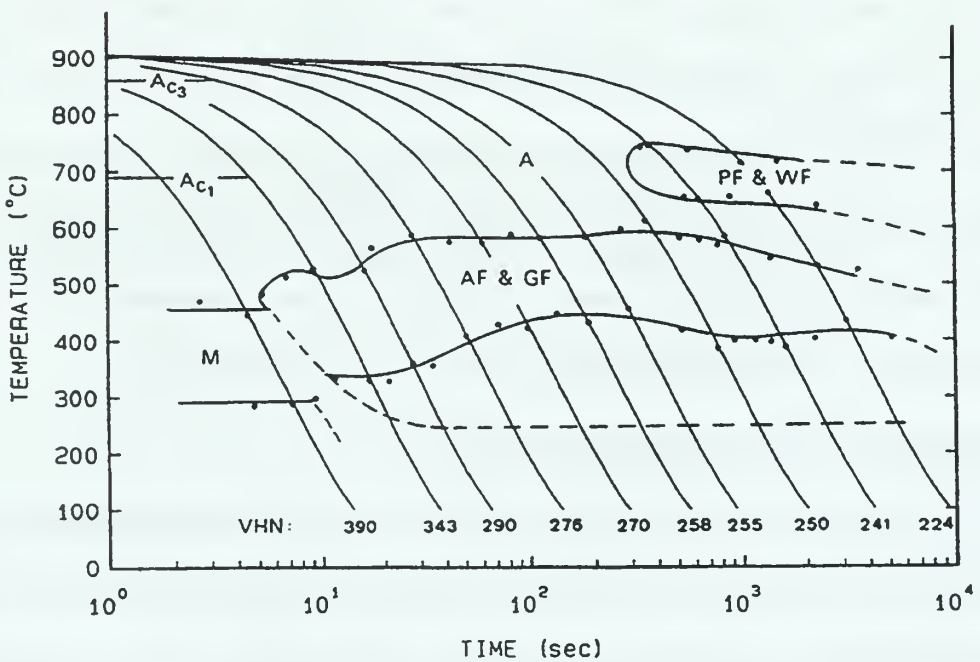

Figure 2-3: Representative continuous cooling transformations diagram for HSLA steel.

1. Primary Ferrite (PF)

Primary ferrite includes both grain boundary ferrite, PF(G), and intragranular polygonal ferrite. This is the initial transformation product as the weld cools from the austenite range into the ferrite range. Grain boundary ferrite, also known as *allotriomorphic* ferrite, nucleates at the prior austenite grain boundaries. Polygonal ferrite, PF(I), nucleates inside prior austenite grain boundaries. Both form an essentially planar interface with the austenite, and the transformation is controlled by the diffusion of carbon from the ferrite to the austenite. Both allotriomorphic and polygonal ferrite are believed to obey the Kurdjumov-Sachs relationship with the austenite grain(s) into which they grow. [Ref. 10] This is believed to be the reason that grain boundary ferrite grows preferrentially into one of the grains that they touch while not growing into the other grain. Primary ferrite forms at higher temperatures and requires slower cooling rates that allow the diffusion of carbon to take place across the planar interface, and this also allows carbon to diffuse into the austenite away from the interface. This prevents carbon buildup at the planar interface, which would impede its movement and promote other mechanisms of transformation from austenite to ferrite. Primary ferrite has been shown to lower the toughness of the weld, and is usually undesirable. [Ref. 11]

2. Acicular Ferrite (AF)

Acicular ferrite gets its name from its microstructure. "Acicular" means shaped and pointed like a needle. It was once thought that acicular ferrite forms tiny non-aligned ferrite needles, but current evidence indicates that the microstructure more likely consists of thin, non-aligned, lenticular plates of ferrite. [Ref. 9] Acicular ferrite nucleates on

non-metallic inclusions inside the prior austenite grains, and is therefore intragranular in nature. These plates of ferrite, which grow out from the inclusions, form an interlocking, basket weave structure. It is from this interlocking structure that acicular ferrite obtains its toughness. The interlocking plates of ferrite impede crack propagation, thereby requiring more energy to allow the propagation to continue. This microstructure typically forms at relatively low temperatures, where diffusion is sluggish, and where the transformation mechanism tends to be displacive. [Ref. 12]

Acicular ferrite has additional benefits in multipass welds. When a weld pass is laid down on top of previous weld passes, the metal in the previous weld passes near the new weld pass will be heated up to a high enough temperature to be reaustenitized. When acicular ferrite in these prior weld passes is reaustenitized, fine equiaxed grains result that improve both strength and toughness. [Ref. 13]

3. Ferrite with Second Phases (FS)

Ferrite with second phases includes those microstructures that have an aligned second phase, FS(A), which include Widmanstätten ferrite, FS(SP), bainite, FS(B), upper bainite, FS(UB), and lower bainite, FS(LB), and those microstructures that have a non-aligned second phase, FS(NA). In the first case, the type of microstructure depends on morphology differences discernable in the scanning electron microscope or transmission electron microscope, but which is normally not discernable in the optical microscope. Widmanstätten ferrite grows when cooling rates are too fast to maintain a planar interface. This results in platelike ferrite growing from the grain boundaries, or from primary ferrite. Due to the faster cooling rates, carbon cannot diffuse away from the

ferrite-austenite interface, and supersaturation occurs on the austenite side. This increases the interface energy, which impedes interface motion and the primary ferrite essentially stops growing. If a "bump" forms in the interface, as shown in Figure 2-4 [Ref. 10], a local increase in the carbon concentration gradient increases the local velocity of the interface and the bump grows faster than the rest of the interface. Side plate ferrite can form faster than primary ferrite because carbon can diffuse away from the front of the plate in several directions instead of just one direction. The width of the plate does not increase significantly because the sides have high interfacial energy, which slows or stops their movement.

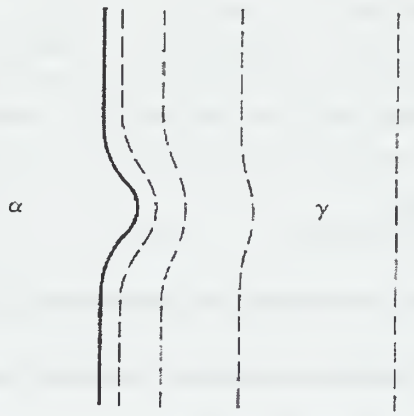

Figure 2-4: α-γ interface showing iso-concentration lines in γ in front of the growing ferrite.

Bainite forms at lower temperatures and faster cooling rates than side-plate ferrite. It consists of fine plates of ferrite, with carbides precipitated either between the plates (upper bainite) or inside the plates (lower bainite). This process occurs too rapidly to be explained by diffusion alone, and is thus believed to result from a mixture of diffusion and shear processes. [Ref. 10] Bainite is hard, due to the fine plates of ferrite, but it

usually has higher toughness than martensite, and in steel welds where it is difficult to get acicular ferrite to nucleate, bainite is desired over primary ferrite or martensite due to its strength and toughness, respectively.

Ferrite with non-aligned second phase is associated with ferrite completely surrounding either microphases or laths of acicular ferrite. [Ref. 8]

4. Ferrite Carbide Aggregate (FC)

Ferrite carbide aggregate includes ferrite with interphase carbides and pearlite. It forms at high temperatures and slow cooling rates than ferrite with secondary phase or martensite. It is a cooperative growth of cementite and ferrite in a lamellar form, and grows out of grain boundary ferrite. Since it is not usually seen in welded steels, due to the slow cooling rates required, it will not be discussed in detail.

5. Martensite (M)

Martensite is associated with very low transformation temperatures and very fast cooling rates. The transformation occurs at temperatures below which the diffusion of carbon is significant and is therefore termed a diffusionless transformation. In low carbon steels, the transformation occurs from fcc_{γ} (austenite) to $bct_{\alpha'}$ (martensite), and mainly involves a defect structure of needles or laths with a high dislocation density. In higher carbon steels, twinning is the defect mainly associated with martensite formation, not dislocations. [Ref. 14] Martensite is very hard and brittle. It is not desired in welds due to its low fracture toughness.

6. Non-Metallic Inclusions

Non-metallic inclusions are formed during the welding process by the interaction of oxygen with elements like aluminum, titanium, manganese, and silicon. Sulfides like copper sulfide (CuS) and manganese sulfide (MnS) may also form if the sulfur content of the weld metal is at or above the soluble limit (~0.003 wt% in steels [Ref. 12]). These oxides and sulfides will float to the surface of the molten metal if allowed enough time, as in steel plate manufacturing, but usually end up trapped in the weld fusion zone due to the rapid cooling rates associated with welding. These inclusions may be involved in two mechanisms that affect the strength and toughness of the weld. First, they can be nucleation sites for acicular ferrite that improves the toughness of the weld as already discussed. Secondly, they can be responsible for the nucleation of cleavage cracks in brittle failure, or the nucleation of voids during ductile failure. [Ref. 12]

Inclusions are classified as exogenous or indigenous depending on their origin. Exogenous inclusions arise from welding slag and surface scale entrapment, while indigenous inclusions form within the weld as a result of deoxidation or solid state precipitation reactions. The latter are usually seen as multiphase, angular or spherical particles, with varying crystallographic properties due to the complex alloying system involved. [Ref. 5] The composition and role of inclusions in the formation of steel plates where melting takes place at or near equilibrium is well understood, but in welding, where cooling rates depart greatly from equilibrium, it becomes more difficult to predict inclusion behavior.

a. Deoxidation

Deoxidation is the process of removing oxygen from the weld pool. This is performed by introducing elements into the weld pool, either from the base metal, or the consumable electrode/flux, or both, that react with oxygen to form non-metallic (oxide) inclusions. This reduces the amount of dissolved oxygen within the weld. Strong deoxidants like aluminum and titanium react to form oxides such as Al_2O_3, TiO, TiO_2, and Ti_2O_3 respectively. Some of these oxide inclusions are favorable nucleation sites for acicular ferrite. Other weaker deoxidizers like silicon and manganese have also been observed in inclusions as SiO_2 and MnO, and have been found to be favorable sites for acicular ferrite formation.

b. Desulfurization

Sulfur is extremely undesirable in steel weld metal because it reacts with iron to form FeS. Due to low surface tension of FeS, it forms a film along steel grain boundaries, and thus greatly reduces a steel weld metal's resistance to solidification cracking. [Ref. 1] To prevent this, manganese levels in the weld are maintained high enough to ensure a Mn:S ratio of at least 12:1 so that MnS forms instead of FeS. This improves solidification cracking resistance and strength because the MnS has a high melting point, and a globular morphology. MnS does not wet the entire grain boundaries of the steel. Instead it forms globules along the grain boundaries, and has been observed as caps on the surface of non-metallic inclusions. Copper can also react with sulfur to form CuS and Cu_2S which do not significantly affect the resistance to solidification

cracking, and which also appears as caps on the surface of inclusions, or as particles inside inclusions.

D. SCOPE OF PRESENT WORK

The Naval Surface Warfare Center, Carderock Division has done significant research aimed at understanding the factors that determine the strength and toughness in high-strength low-alloy steel welds, and to quantify these factors using regression analysis methods. [Ref. 15] Their research included fifty-two welds that were fabricated using seven different solid weld wires and the GMAW process (spray or pulsed) with a shielding gas of 95% Ar and 5% CO_2. Since microstructural features are difficult to measure and correlate with mechanical properties, the 50% transformation temperature, which can be experimentally obtained, was used to correlate with mechanical properties. A model for determining the 50% transformation temperature was developed based on the cooling rate, weld metal carbon, molybdenum, nickel contents, and the ratio of the weld metal silicon to oxygen contents. A model was also developed to predict the prior austenite grain size based on the weld metal oxygen, molybdenum, and nickel contents. It was observed here that on passing through T_{50} = 510°C, the dependence of the prior austenite grain size on the above elements changes, and therefore two models were needed. [Ref. 15]

The two models above were used to develop models for strength and toughness of the weld metal. Again, there was a change in the behavior of the models at a T_{50} of about

510 °C. It was determined from these results that at $T_{50} \leq 510°C$, the microstructure contained significant amounts of martensite, whereas for $T_{50} > 510°C$, there was not much martensite present. Additionally, it was determined that the 50% transformation temperature is a good indicator of the microstructure type and this was successfully correlated with the weld deposit strength. The details of these models will be discussed in the Results and Analysis section.

Ten of the fifty-two weldments will be studied in the present work in order to correlate the microstructure, and the average non-metallic inclusion diameter and volume fraction with the strength and toughness of the weld. The chemical composition of the non-metallic inclusions and the metal-inclusion interface will also be analyzed in order to shed additional light on how the inclusions affect the microstructure and the mechanical properties of the weld. This data will also be used to try and understand the scientific basis for the model developed by NSWC.

III. EXPERIMENTAL PROCEDURE

A. SAMPLE PREPARATION

Ten polished and etched samples were received from NSWC encased in epoxy mounts. They also had surface indentations that resulted from micro-hardness testing. The samples were ground on a Struers Knuth-Rotor-3 grinder using Buehler 600 and 2400 grit wet/dry silicon-carbide grinding discs. They were then polished on an Ecomet 4 variable speed grinder-polisher using Buehler micro-cloth and Buehler Metadi 3 micron and 1 micron water based diamond suspensions. The samples were cleaned with a soap-water mixture in between grinding/polishing, and were soaked in an ultrasonic acetone bath after final polishing to ensure cleanliness.

For optical microscopy, the samples were etched with Nital (5% Nitric acid, 95% Methanol) for ten seconds and rinsed in methanol. For scanning electron microscopy, the polished samples had to be painted with a silver suspension to allow proper grounding and prevent electrically charging the samples. This was required since the epoxy mounts are non-conductive.

Carbon replicas of all ten samples were made in order to analyze the chemical makeup of the non-metallic inclusions without interference from the weld metal. The samples were deep etched in Nital (5% Nitric Acid 95% Methanol) for 20 seconds and then coated with carbon using a No. 12560 EFFA Mk II Carbon Coater. Two strands of carbon fiber were used with a working distance (distance from the fibers to the sample

surface) of 3 cm. The mechanical pump was used to draw a vacuum of 200 millibars. Each sample was flashed 3-5 times, resulting in a bluish-gold color representing a thickness of about 20 nm. Three-millimeter square sections were scribed into the surface of each sample, and they were again deep etched in Nital until the carbon coating began to lift off of the sample. One three-millimeter square carbon layer was lifted out of the Nital using a flat tipped instrument, and placed in a 5% Acetone, 95% water bath. The acetone bath straightened out the carbon film due to surface tension effects. The carbon films were lifted out of the acetone bath using 200 mesh copper grids. Previous work used nickel grids because of the possibility of copper-sulfide being present in the inclusions, but the sulfur content in nine of the ten samples was at or below the soluble limit (0.003 wt%) [Ref. 12] of sulfur in steel, so it was not deemed a necessary precaution. The grids with the samples were then dried for about 30 minutes under a 40-watt desk lamp and placed into a sample holder. Figure 3-1 steps through the carbon extraction replica procedure.

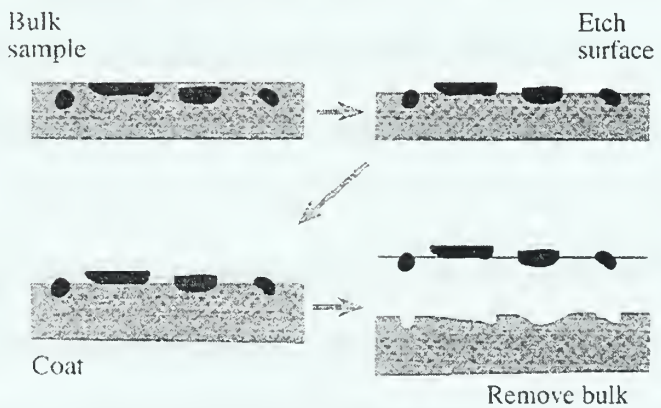

Figure 3-1: Extraction replication. Particles embedded in the matrix are revealed by etching; a thin amorphous carbon film is evaporated over the particles; the rest of the matrix is etched away leaving the particles adhering to the carbon film. [Ref. 16]

One sample was selected to produce a thin foil sample from (PD 21092 S1) for analysis in the transmission electron microscope. To start with, this sample was removed from its epoxy mount, and a 700-micron section was removed from it. The section was then thinned to about 10-15 microns using the Struers Knuth-Rotor-3 grinder and Buehler 320, 500, 1000, and 4000 grit wet/dry sandpaper. A 3-mm sample was removed from the section using a punch. This sample was electro-polished using a twin jet model 110 electro-polisher until it developed a tiny hole in the center (the metal near the hole is thinned to only a few atoms thick and is suitable for transmission electron microscopy).

B. OPTICAL MICROSCOPY

1. Microscope Description

A Jenaphot 2000 Reflected-light Photomicroscope was used to obtain optical images of the etched samples. It is an inverted-type (sample is placed on top of the specimen plate and faces down), bench top, high precision microscope with a tilting binocular head for viewing height adjustment. It has a motorized objective lens system that allows changing of objectives independent of the objective's working distance. A high-resolution video camera was used to capture images of the samples using Semicaps Genie 1.0 Desktop Imaging System. Figure 3-2 shows the layout of the microscope and imaging system.

2. Point-Count Method

Ten random photo images from the center of the fusion zone (Charpy sample) of each sample were captured at 500X in order to determine the amount of acicular ferrite present. The final weld passes were not included in the samples because they may contain more acicular ferrite than the rest of the weld since none of it is reaustenitized and it is from multi-pass regions from the center of the weld from which the mechanical properties data were obtained. These images were printed as 4.5 inch by 6 inch photographs on a Hewlett-Packard 870 Cse Professional Series printer. These photographs were used to determine the percent acicular ferrite (%AF) in each sample using ASTM standard E 562-89 as a guide. The ASTM standard was not followed in choosing the number of grid points per volume fraction being analyzed, or in statistical analysis. [Ref. 17,18] Each photograph was overlaid with a grid of 63 points resulting in a total of 630 points for each sample. The percent acicular ferrite was determined by dividing the number of points that fell on top of acicular ferrite by the total number of points.

The following binomial equation was used to calculate the standard deviation in lieu of ASTM Standard E 562-89:

$$\sigma^2 = p(1-p)/n \tag{3.1}$$

where,

σ = standard deviation
p = proportion of phases being analyzed
n = number of grid points [Ref. 18]

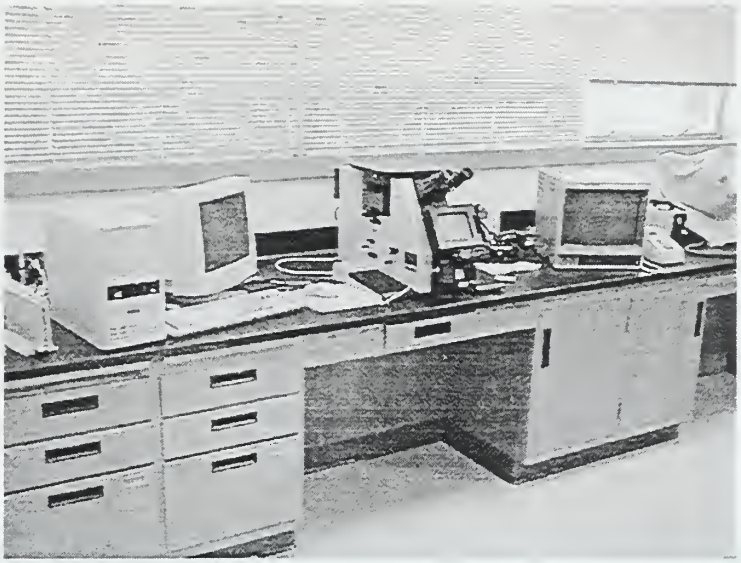

Figure 3-2: Jenaphot 2000 Reflective-light Photomicroscope and associated imaging system.

Figures 3-3 and 3-4 show photomicrographs of representative fusion zone microstructure that were used to determine the percent acicular ferrite present. Table 3-1 shows the percent acicular ferrite (%AF) and the standard deviation for each sample.

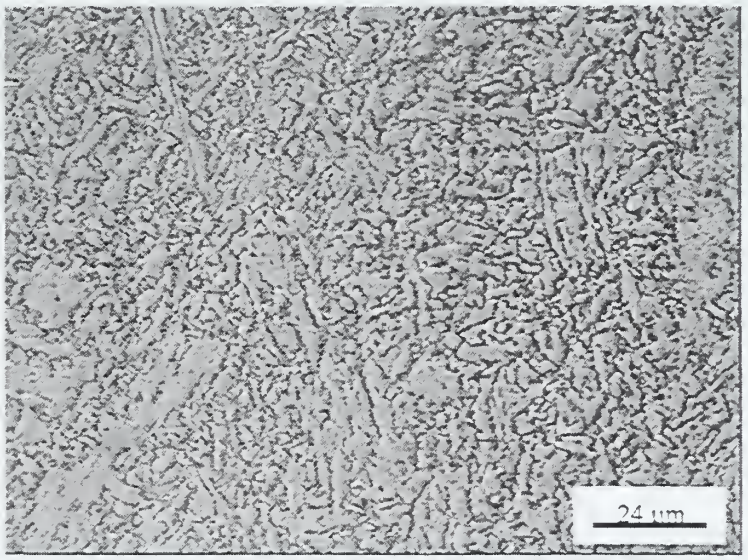

Figure 3-3: Representative fusion zone microstructure PD 21150.

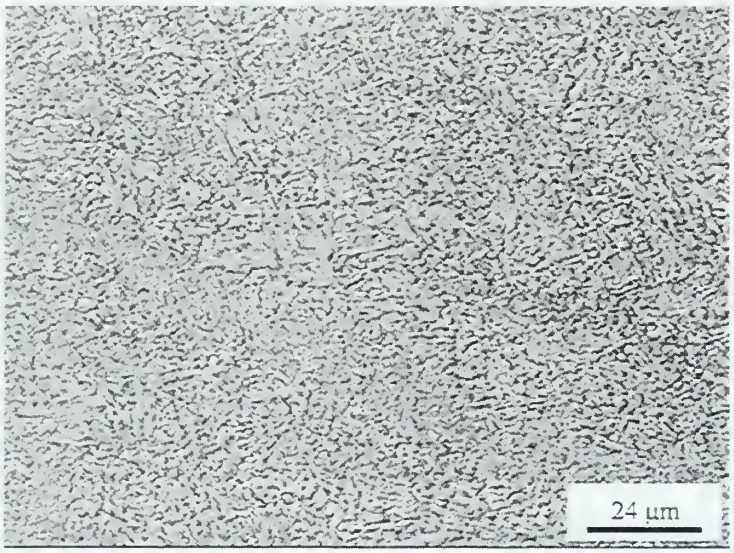

Figure 3-4: Representative fusion zone microstructure PD 21251 S2.

Sample ID	%AF (95% confidence)	Standard Deviation
PD 21092 S1	15.397 ± 0.8335	1.438
PD 21092S2	15.236 ± 0.8300	1.432
PD 21149	8.255 ± 0.6352	1.096
PD 21150	10.318 ± .07025	1.212
PD 21151	9.842 ± 0.6880	1.187
PD 21151 S2	14.603 ± 0.8156	1.407
PD 21176	8.096 ± 0.6301	1.087
PD 21242	10.794 ± 0.7164	1.236
PD 21251 S2	17.778 ± 0.8828	1.523
PD 21255	5.396 ± 0.5217	0.900

Table 3-1: Weld metal acicular ferrite percentages

C. SCANNING ELECTRON MICROSCOPY

1. SEM Overview

All ten samples were analyzed in a Topcon SM-510 Scanning Electron Microscope (SEM). Figure 3-5 shows the layout of the SEM and Figure 3-6 shows a schematic of a typical SEM.

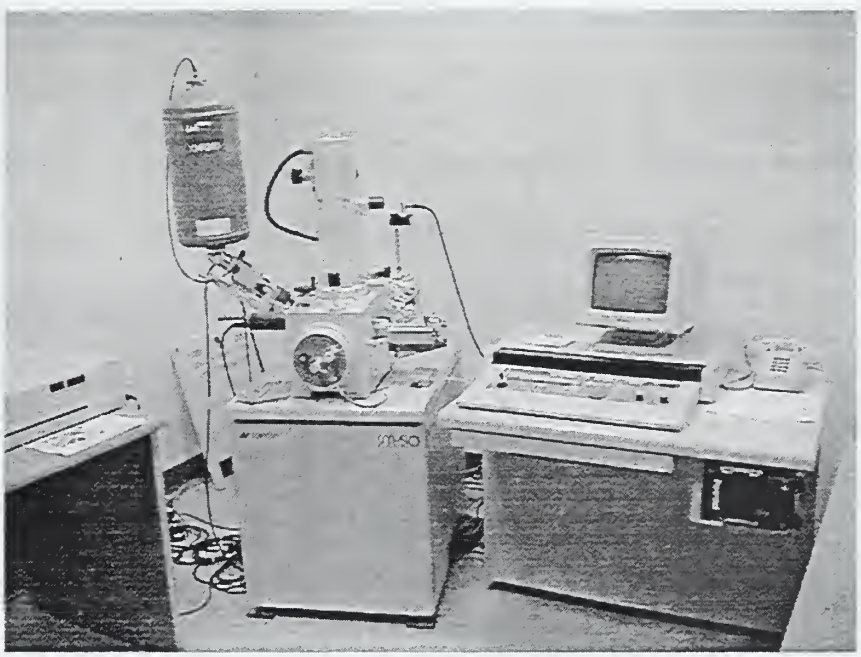

Figure 3-5: Topcon SM-510 Scanning Electron Microscope.

The microscope consists of an electron gun, condenser lenses, scanning coils, objective lens, collector, photomultiplier and amplification circuit, and the display. The electron gun consists of a filament that emits electrons when heated. These electrons are condensed into a tight beam by the condenser coils. The electron beam is rastered over

the sample surface by the scanning coils. The objective lens is used to focus the electron beam on to the sample.

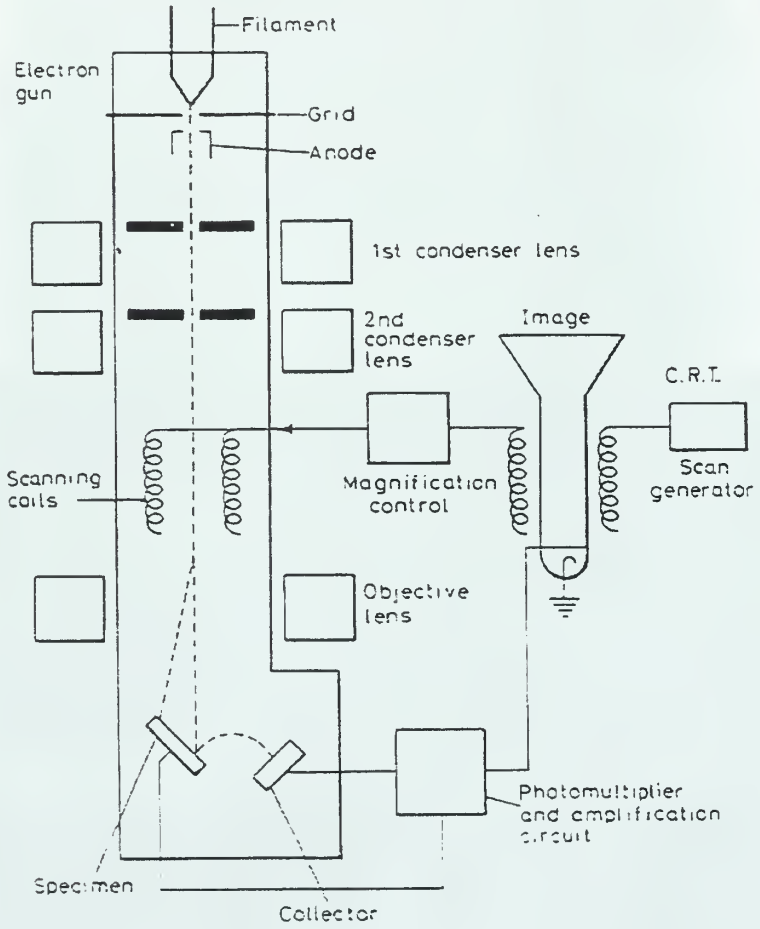

Figure 3-6: Schematic of a typical SEM.

When the electrons impact the sample surface, several things happen. First, some of the high-energy electrons bounce off of the sample, or backscatter. The electron beam can also knock electrons that were orbiting atoms out of their orbits and free from the atoms. These electrons are secondary electrons and have lower energy than the incident beam. The incident beam can also interact with atoms to raise their electrons to higher orbital shells. When the electrons drop back down to their lower energy states, either x-

rays are emitted or the energy is transmitted to a neighbor electron that breaks free from the atom (Auger electrons). Figure 3-7 displays the typical reactions that take place in an SEM. Figure 3-8 shows a schematic of the area of interaction of electrons in a thick SEM sample.

The collector (positively charged to attract the low energy electrons in the secondary electron mode, and negatively charged to prevent saturation with high-energy electrons in the backscatter mode) collects backscattered and secondary electrons. The current is converted to light pulses and amplified in the photomultiplier and amplification circuit. This light signal is used to adjust the brightness of an oscilloscope spot that is synchronized with the electron beam at the sample surface. The image is displayed on an oscilloscope screen. The x-rays and Auger electrons can be collected to give information on the chemical composition of the sample.

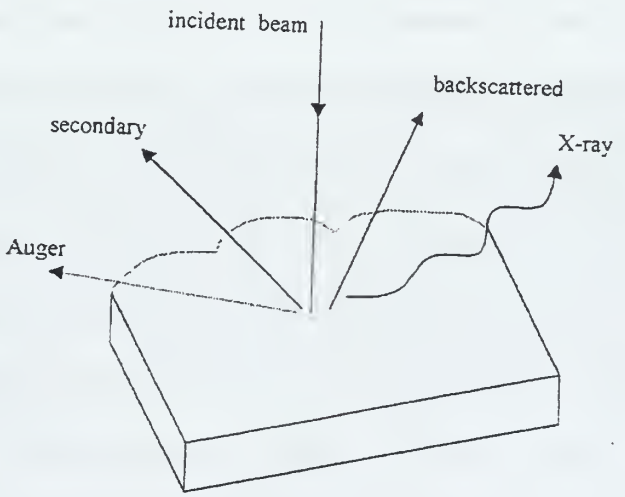

Figure 3-7: Electron interactions in an SEM sample. [Ref. 18]

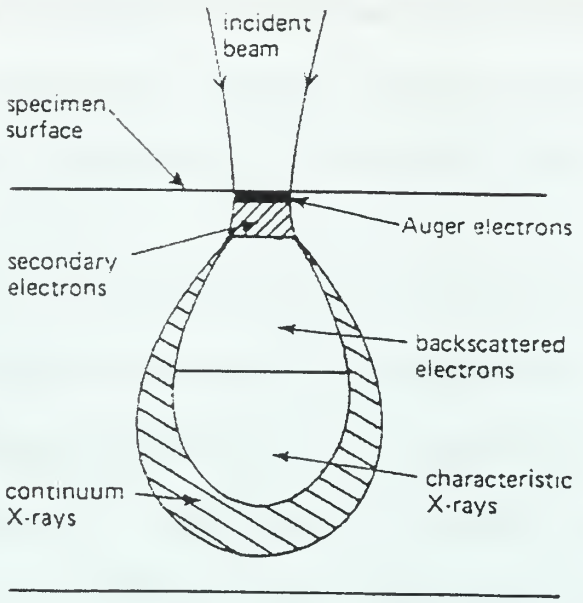

Figure 3-8: SEM bulb of interaction. [Ref. 19]

2. SEM Procedure

One hundred random secondary electron images of each sample were captured using the Link Isis and Link Tetra software on a 486/DX2 computer. The SEM was operating at 20KV with a 28mm working distance and a magnification of 5000X. Secondary electrons were selected because they emerge from nearer the surface than backscatter electrons, providing a more two-dimensional image that is required for area-fraction determination (see Figure 3-8). The use of backscattered electrons would produce a more three-dimensional image, and would not give an accurate area-fraction. These images were used to determine the average diameter and volume fraction of non-metallic inclusions for each sample. Figures 3-9 and 3-10 show typical SEM images of two different samples (PD 21150 and PD 21251 S2).

3. Diameter and Volume Fraction

The diameters of the non-metallic inclusions were measured using Microsoft Publisher's built-in measuring tool. A mean inclusion diameter and standard deviation were calculated using Microsoft Excel.

The volume fraction was assumed to be about the same as the area fraction. This is a valid assumption only when the probability of looking at any plane in the sample is the same (i.e., the probably of polishing any plane in the sample is the same). [Ref. 20] The volume fraction was determined by calculating the area of each inclusion ($A = 2\pi r$), adding up the areas of all of the inclusions in a field, and dividing the sum by the total area of a field (429.4μm). A mean volume fraction was calculated by averaging the volume fractions of all of the fields for each sample. Appendix A shows the volume fractions and mean diameters of non-metallic inclusions, and appendix B shows the distributions of the non-metallic inclusion diameters (histograms).

Figure 3-9: Typical SEM image (PD 21150)

Figure 3-10: Typical SEM image (PD 21251 S2)

D. TRANSMISSION ELECTRON MICROSCOPY

1. TEM Overview

The carbon extraction replicas (see sample preparation) were analyzed in the Topcon 002B TEM operating at 200KV. Figure 3-11 shows the Topcon 002B TEM. The TEM operates similarly to the SEM, except that higher spatial resolution can be achieved (0.18 nm [Ref. 21]) because the higher energy electrons have a shorter wavelength and thin samples are used.

The TEM consists of an electron gun, condenser lenses, sample holder, objective lens, objective aperature, SAD aperature, intermediate lens, projector lens, and a fluorescent viewing screen (see Figure 3-12). As with the SEM, the electron gun emits electrons upon heating, and the condenser coils condense the electrons into a fine beam

or probe. The sample is mounted above the objective lens, since the electrons that are used to display the image go through the sample. This is different than the SEM where the electrons were collected on the same side of the sample as the incident beam. Figure 3-13 shows typical TEM thin foil electron interactions.

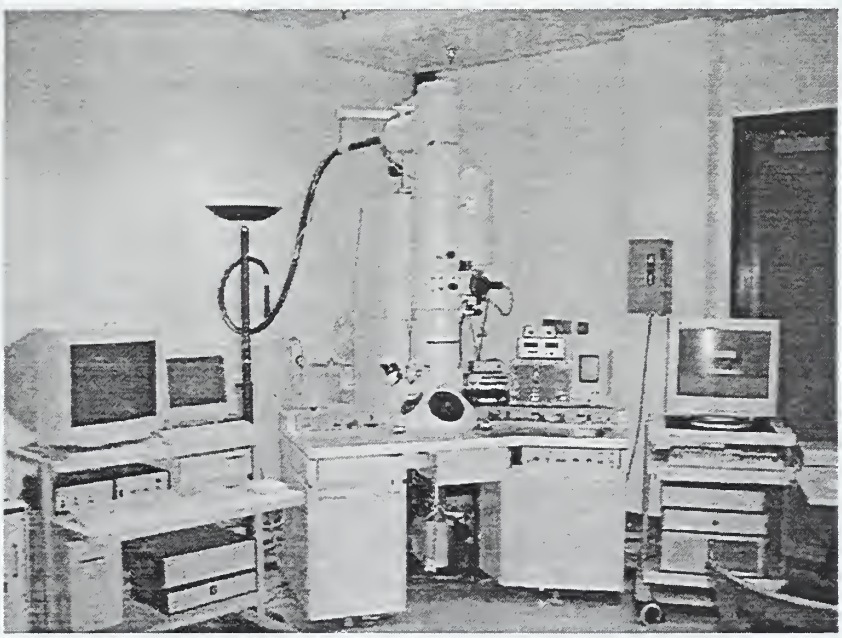

Figure 3-11: Topcon 002B Transmission Electron Microscope.

Below the objective lens, there are two apertures: the objective lens aperture and the Selected Area Diffraction (SAD) aperture. These apertures allow viewing an image of the sample, or the diffraction pattern of a selected area of the sample depending on their positions. Electron diffraction is useful in determining crystallographic orientation.

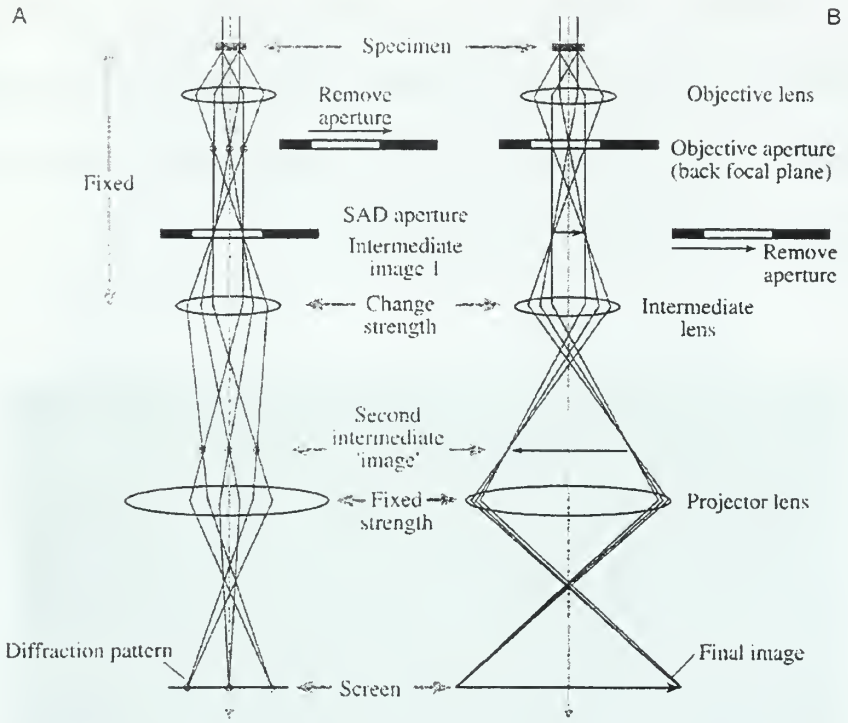

Figure 3-12: TEM schematic projecting a (a) diffraction pattern and (b) image. [Ref. 16]

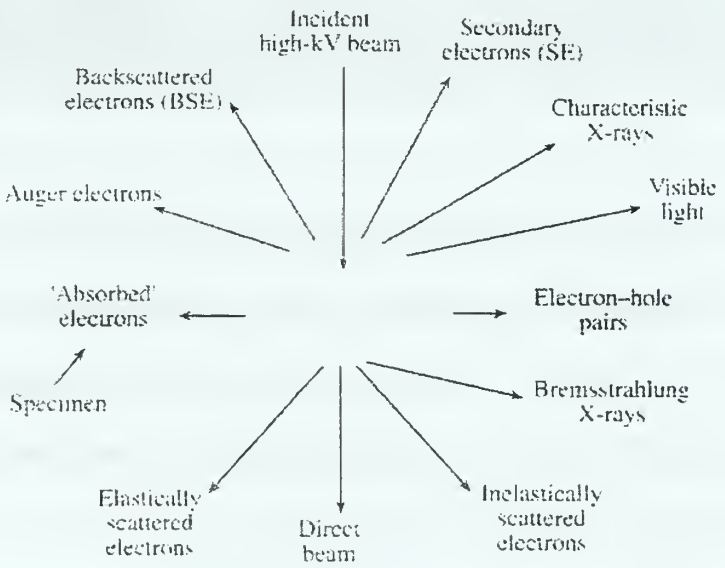

Figure 3-13: TEM thin foil electron interactions. [Ref. 16]

2. Energy Dispersive X-ray Spectroscopy (EDX/EDS)

As seen in Figure 3-13, and as explained in SEM overview, characteristic x-rays result when electrons interact with elements. These x-rays can be counted using a lithium drifted silicon (LiSi) detector. The detector generates voltage pulses that are proportional to the energy of the x-ray. The pulses are processed and analyzed and displayed using ES Vision 3.1 as intensity (counts) vs. energy level. Because the x-rays have characteristic energy levels, the elements that produce them can be determined based on the energy levels of the peaks in the display. The fraction of each element that is present can also be determined based on the intensity. Smallman gives the relationship between the intensities of two elements A and B as:

$$\frac{n_A}{n_B} \propto \frac{I_A Q_B \omega_B a_B \eta_B}{I_B Q_A \varpi_A a_A \eta_A} = K_{AB} \frac{I_A}{I_B} \tag{3.2}$$

where,

n = number of atoms
Q = ionization cross sections
ω = fluorescent yields
a = fraction of K lines collected
η = detector efficiencies [Ref. 19]

Equation (3.2) is the basis for EDX quantification. K_{AB} is known as the Z-correction and contains the factors needed to correct for atomic number differences. [Ref. 19]

The EDX graph must be corrected for background radiation. This is done by selecting background energy windows and using a second order polynomial background correction scheme that is built into the software. The other corrections that are done during quantification are for sample thickness and density, which were assumed to be 100 nm and 4.414 grams per cubic centimeter (average of the densities of MnO and SiO_2),

respectively. Figure 3-14 shows a typical EDX spectrum. Appendix C shows inclusion chemistry data for each sample.

ES Vision 3.1 can also be used in conjunction with the TEM to produce a qualitative map of an inclusion, showing the distribution of elements in the inclusion. This is qualitative only, but can be used as a tool to estimate what compounds are present. Figure 3-15 shows an EDX map of two non-metallic inclusions in close proximity of each other (from sample PD 21251 S2).

3. Thin Foil Sample

The thin foil sample (PD 21092 S1) was analyzed in the TEM to determine the microstructure. The TEM was operating at 200KV with a magnification of 24000X. The microconstituents of concern are lath ferrite, acicular ferrite, and martensite. These microstructures are difficult to see in the optical microscope because of their fineness, but they are easy to identify in the transmission electron microscope.

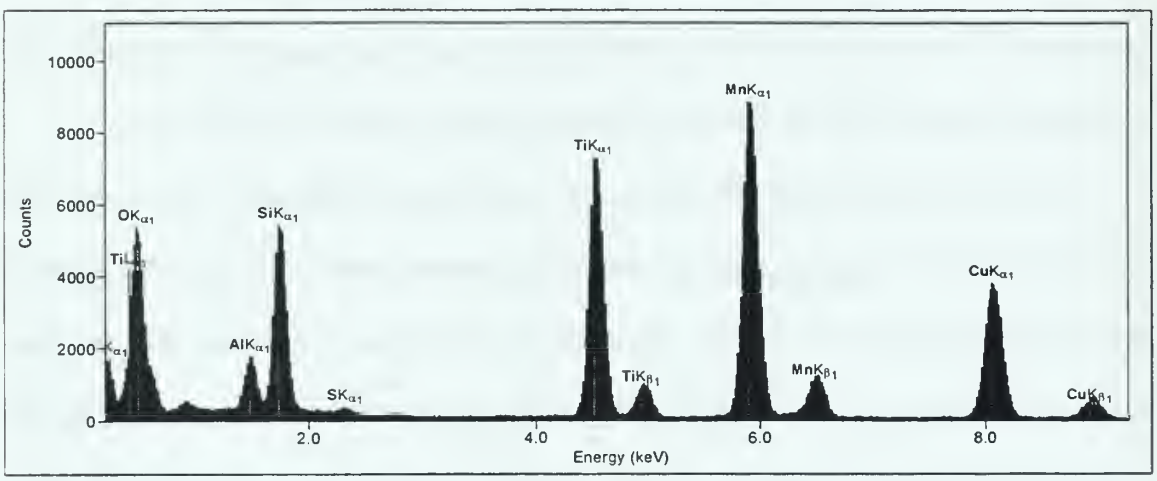

Figure 3-14: Typical EDX spectrum (PD 21251 S2)

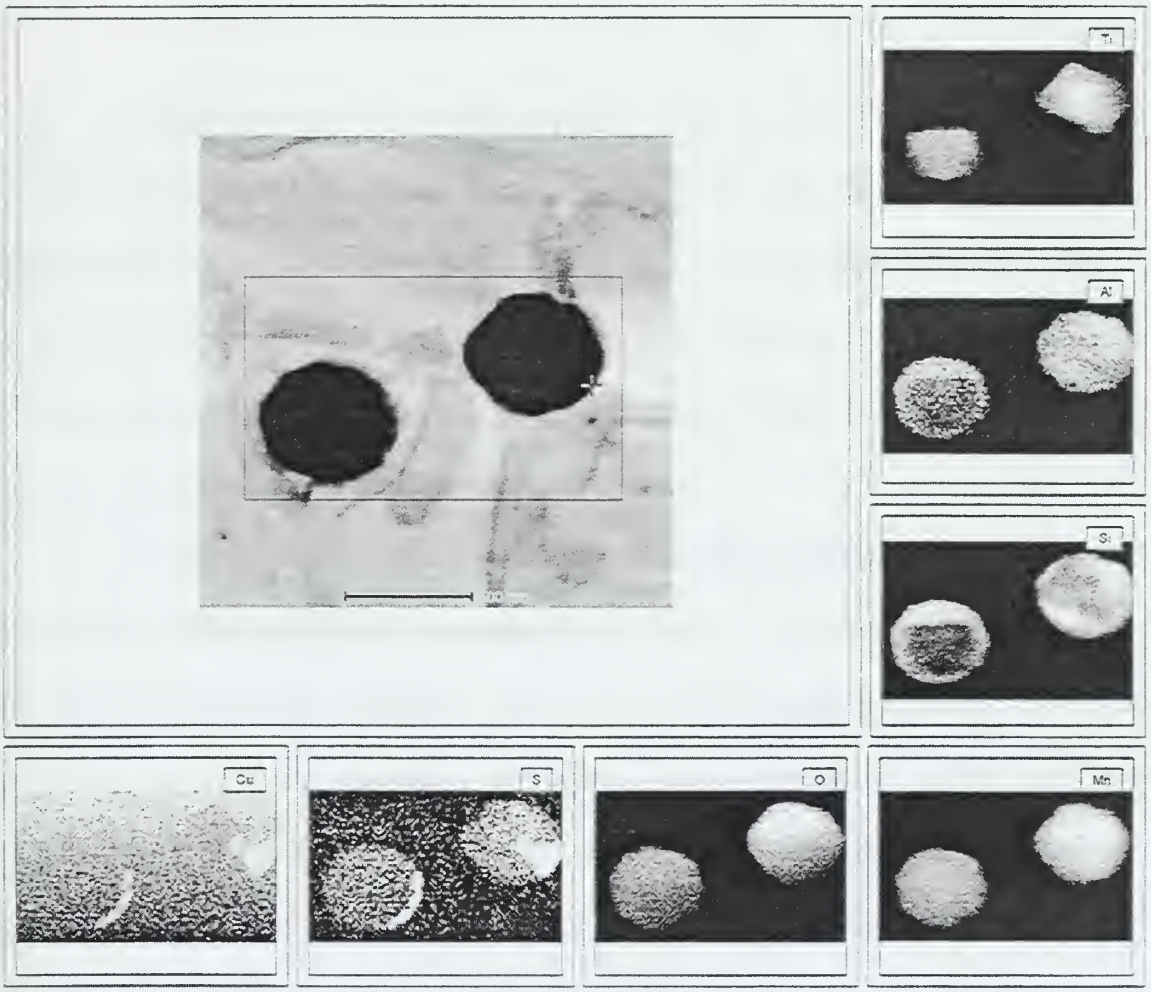

Figure 3-15: EDX mapping of two non-metallic inclusions (PD 21251 S2)

E. ERROR

The error bars on all graphs are based on the following equations, which were used to calculate the 95% confidence intervals for large (>30) or small (<30) sample sizes:

$$\mu = \bar{x} \pm 1.96 \frac{S_x}{\sqrt{n}} \tag{3.3}$$

$$\mu = \bar{x} \pm t_{\alpha,v} \frac{S_x}{\sqrt{n}} \tag{3.4}$$

where,

μ = true mean value
$\bar{x}$ = calculated mean value
S_x = standard deviation
n = sample size
α = 1-c
v = (n-1) degrees of freedom
t = distribution, small size [Ref. 6, 22]

IV. RESULTS AND ANALYSIS

A. WELD METAL MICROSTRUCTURE

The microstructure within the multi-pass welds consists of varying amounts of grain boundary ferrite, polygonal ferrite, acicular ferrite, lath ferrite, and martensite. Blackburn determined that the progression from large grained polygonal ferrite (Figure 3-3) to a very fine martensitic structure (Figure 3-4) correlates to a decrease in the 50% transformation temperature. He also found that martensite was only present in significant amounts in samples that have a $T_{50} \leq 510°C$. [Ref. 15]

A similar relationship can be seen between the percent acicular ferrite in the weld metal and the 50% transformation temperature. Figure 4-1 shows that as T_{50} increases, the percent acicular ferrite decreases. This can be explained using Blackburn's model for predicting the 50% transformation temperature, which depends on cooling rate, and carbon, nickel, and molybdenum concentrations. [Ref. 15] Higher cooling rates suppress primary and Widmanstätten ferrite in favor of acicular and granular ferrite as shown in Figure 2-3. The vertical lines are lines of constant cooling rate, and the cooling rate increases to the left. Alloying elements like nickel and molybdenum shift the continuous cooling transformation curves to the right, allowing acicular ferrite and granular ferrite to form over a wider range of cooling rates, and making primary ferrite and Widmanstätten ferrite less likely (Figure 4-2).

Acicular ferrite is not believed to directly contribute to toughness in multi-pass regions of ultra-low carbon steel welds performed using the GMAW process and ultra-low carbon filler wire because, as shown in table 3-1, the amount of acicular ferrite present in the weld metal is very low. However, multi-run regions may have had a higher acicular ferrite content before reaustenitization and thus a finer microstructure. Even without significant amounts of acicular ferrite, all of the samples except PD 21150 met the MIL-100S requirements for strength and toughness. [Ref. 3]

Sample PD 21150, which has the lowest strength and toughness, had the largest prior austenite grain size, highest oxygen content, and slowest cooling rate. These factors result in a microstructure that consists mostly of coarse polygonal and grain boundary ferrite without any appreciable martensite.

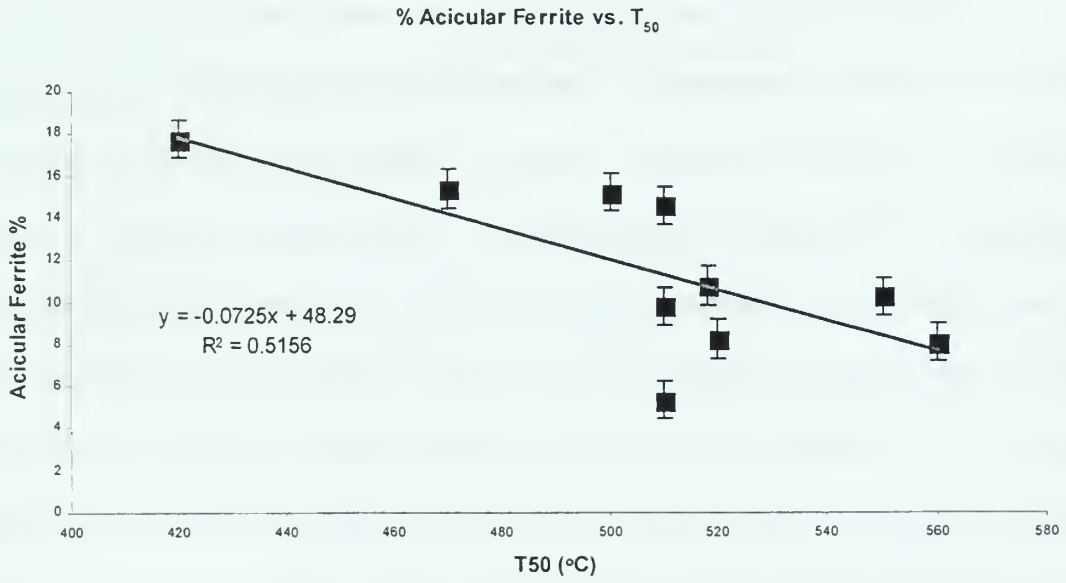

Figure 4-1: Percent acicular ferrite vs. 50% transformation temperature.

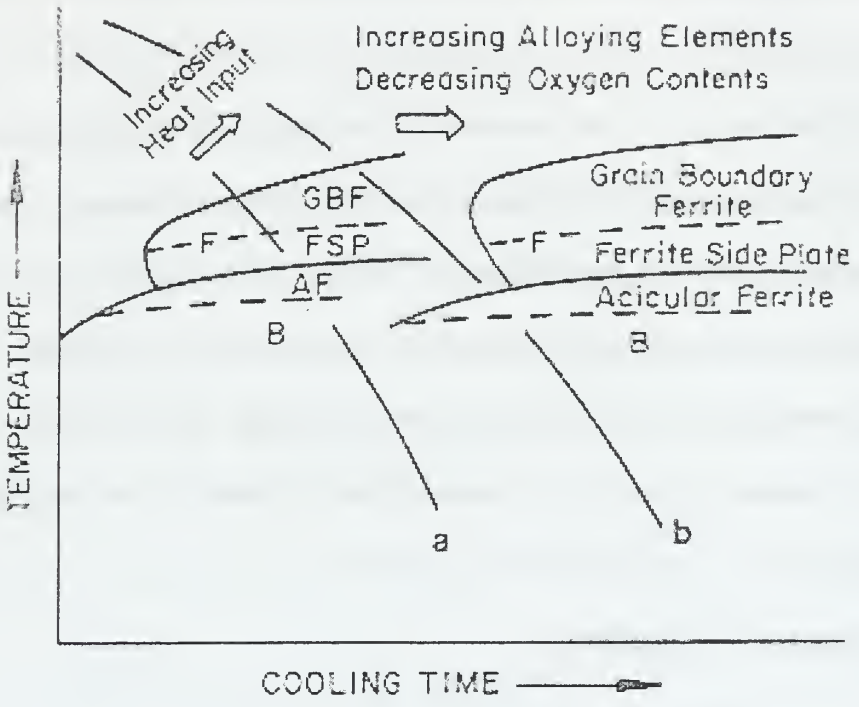

Figure 4-2: CCTD for low carbon, low alloy steel. [Ref. 1]

B. NON-METALLIC INCLUSIONS

1. Non-Metallic Inclusion Size and Volume Fraction

If the non-metallic inclusions are not responsible for forming significant amounts of acicular ferrite in the welds studied, it would be desirable to minimize the size and volume fraction of these since they are responsible for the nucleation of cleavage cracks in brittle failure, or the nucleation of voids during ductile failure. All of the samples have a very small mean inclusion diameter (< 0.3 μm) and a small volume fraction of inclusions (< 0.12 %). To try and understand how this goal was achieved, the

dependency of inclusion size and volume fraction on weld chemistry and heat input must be understood.

It has been shown in previous work that increasing cover gas oxygen content will increase weld metal oxygen content which will in turn increase the average non-metallic inclusion size (diameter) and volume fraction. [Ref. 6] This is believed to be due to the fact that more oxygen is available for deoxidation reactions during welding resulting in more oxides (non-metallic inclusions) of larger size. Figure 4-3 shows that the average diameter of inclusions increases with increasing oxygen content in the weld metal. This figure contains a lot of scatter, which is believed to be due to the non-equilibrium conditions associated with welding.

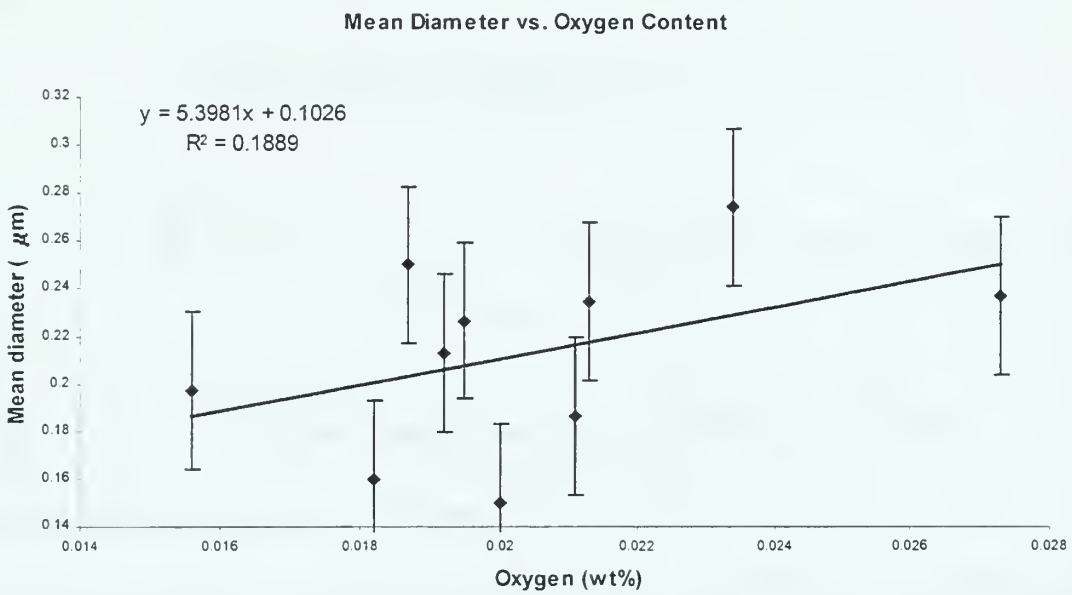

Figure 4-3: Non-metallic inclusion mean diameter vs. weld metal oxygen content.

Figure 4-4 shows that the volume fraction of inclusions increases with increasing oxygen content in the weld. In the case of volume fraction, it is easy to see a segregation

of the data, which may or may not be significant as the error bars are rather large. In Figure 4-4, HSLA-100 samples are represented by the HSLA-100 series while HSLA-80 samples are represented by both the HSLA-80 and HSLA-802 series. The HSLA-100 samples have lower inclusion volume fractions than HSLA-80 samples. The interesting thing to notice is that the HSLA-100 and HSLA-802 series both form linear trends with very good curve fitting, and that these two trends are almost parallel. Samples PD 21242 and PD 21255 had higher volume fractions of inclusions than is predicted by the trend represented by the rest of the HSLA-80 samples.

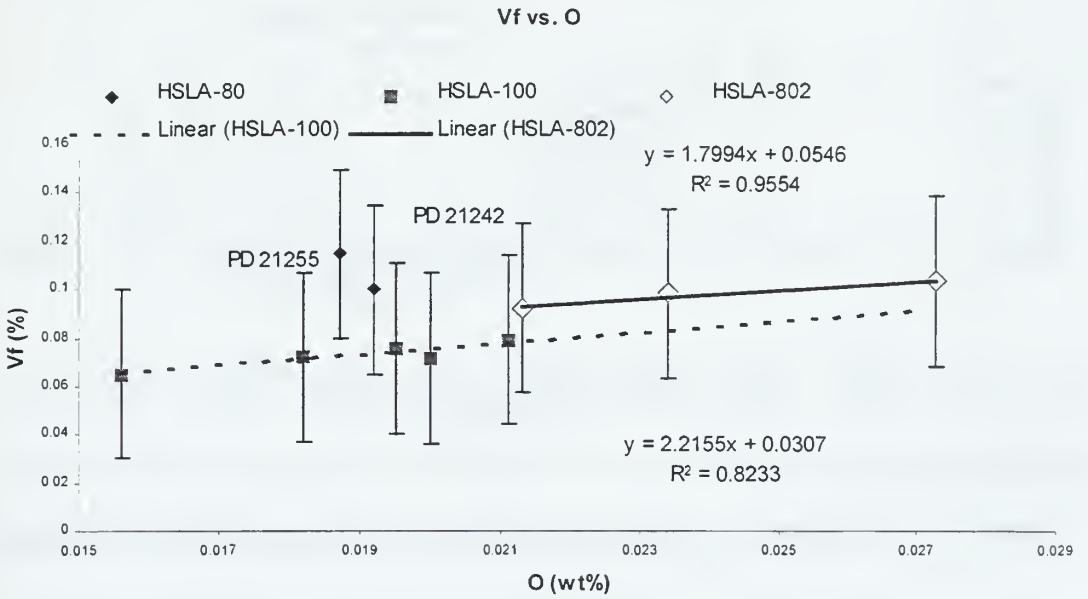

Figure 4-4: Non-metallic inclusion volume fraction vs. weld metal oxygen content.

The non-metallic inclusion size and volume fraction also show a dependence on the amount of deoxidants present in the weld metal. Since aluminum, titanium, and silicon are the three strongest deoxidants present, they were the only ones considered.

Figure 4-5 shows the dependence that the inclusion mean diameter has on the sum of the weight percent of titanium and aluminum in the weld metal. This graph shows the same type of segregation between HSLA-80 and HSLA-100, and two trends can be seen. According to the figure, the inclusion size reaches a minimum value around 0.011 wt% Ti + Al. If the titanium and aluminum are separately graphed against inclusion size, they both demonstrate trends similar to Figure 4-5 (both show a local minimum).

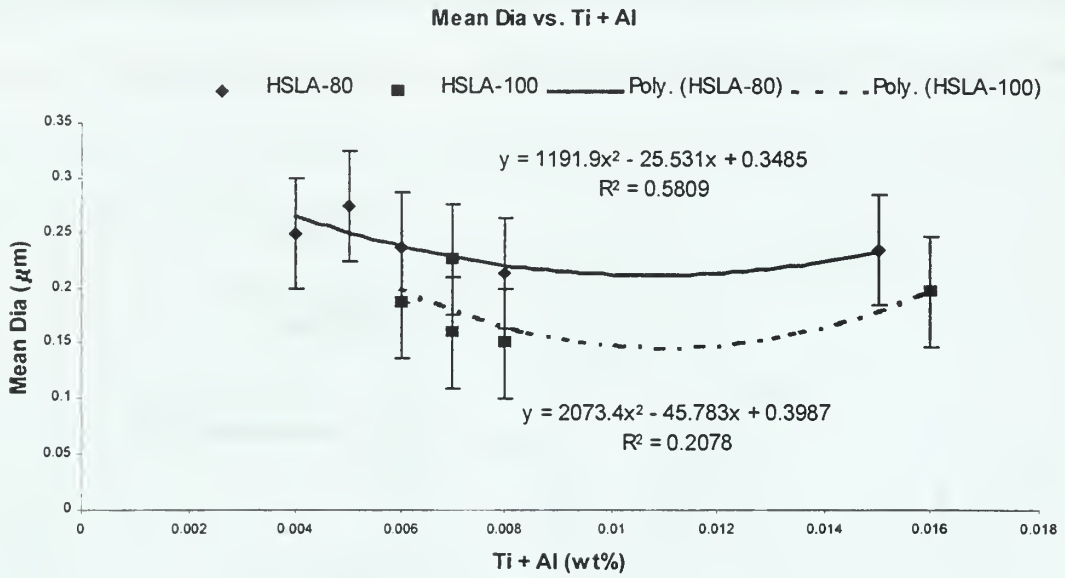

Figure 4-5: Non-metallic inclusion mean diameter vs. weld metal Ti and Al content.

Figure 4-6 shows that the volume fraction of non-metallic inclusions decreased linearly with an increase in the sum of the weld metal titanium and aluminum concentrations. Again, the same segregation that was present in Figures 4-4 and 4-5 can also be seen here. The volume fraction does not reach a minimum value, at least in the range that the samples represent. This indicates that to minimize the volume fraction of

inclusions, increasing the amounts of titanium and aluminum in the weld metal is necessary.

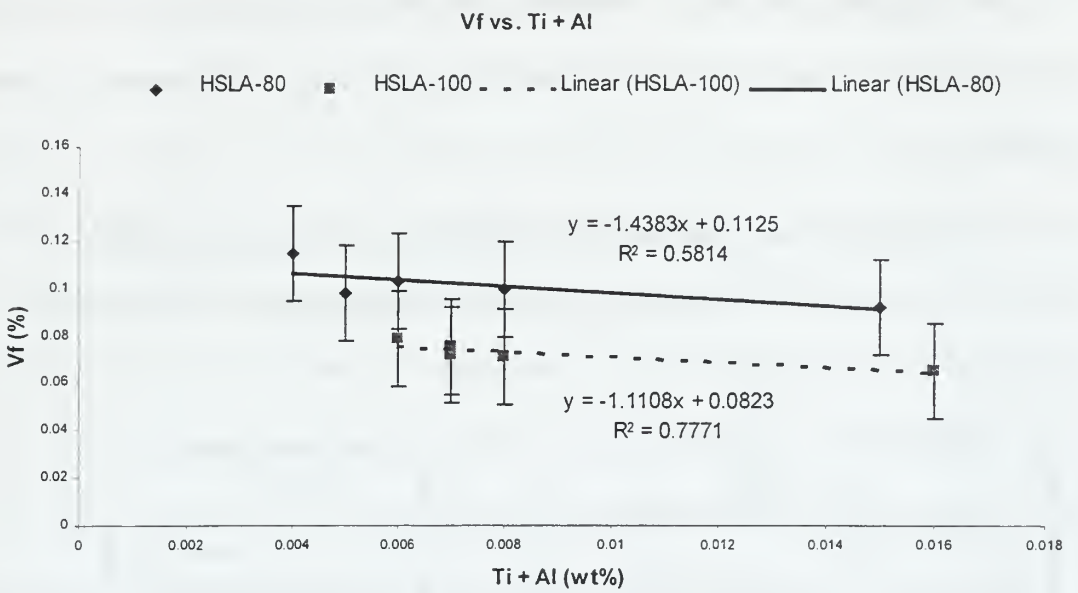

Figure 4-6: Non-metallic inclusion volume fraction vs. weld metal Ti and Al content.

Figure 4-7 shows that the non-metallic inclusion size and volume fraction both decrease with increasing silicon concentration in the weld metal. Segregation between HSLA-80 and HSLA-100 is not observed in this case.

Since the concentrations of aluminum and titanium in the weld metal had different affects on the inclusion size and volume fraction, the affects of the inclusion size and volume fraction on the weld metal toughness were examined to try to determine which had more of an effect on toughness. Due to the scatter in the data, which almost certainly occurs because of the very small inclusion sizes and volume fractions, definite trends were not obtainable from the data. It has been shown by Blackburn et al. [Ref. 23] that increasing the inclusion size and the inclusion volume fraction both result in lowering the

toughness of the weld, but they did not indicate whether volume fraction or inclusion size had a stronger effect. It appears from Figure 4-7 that increasing the silicon concentration in the weld metal (at least over the range analyzed) will help minimize the non-metallic inclusion size and volume fraction. This is to be expected as silicon is also quite a strong deoxidant.

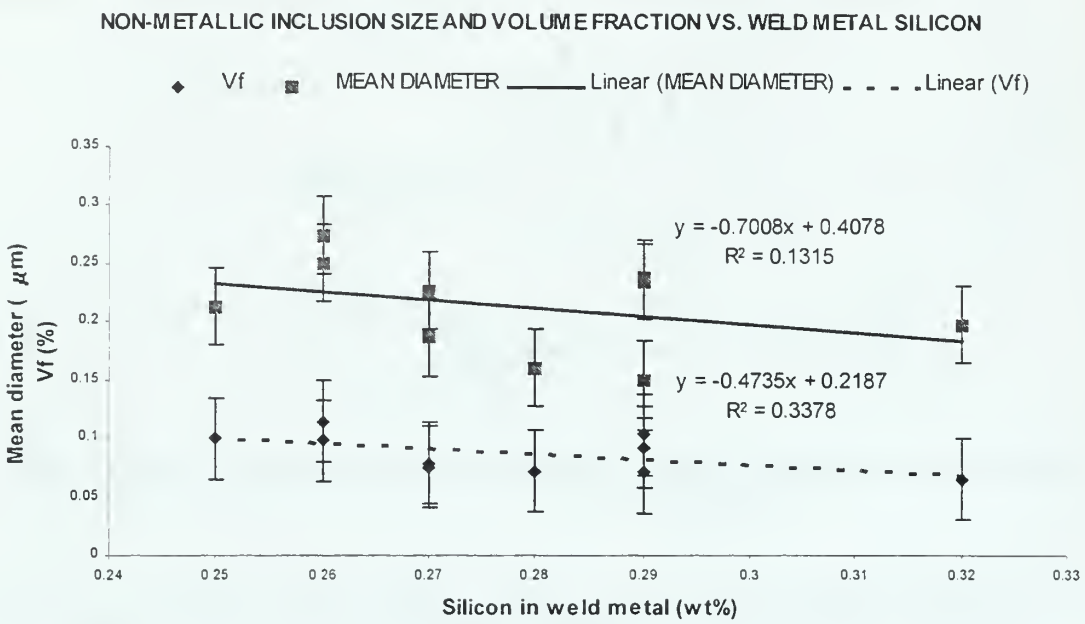

Figure 4-7: Non-metallic inclusion size and volume fraction vs. weld metal silicon concentration.

The non-metallic inclusion size and volume fraction also depend upon the heat input and plate thickness. It is convenient to reduce these two parameters in to a single parameter that represents both, for example, cooling rate. Cooling rate can affect the inclusion size and volume fraction because it determines the amount of time that deoxidation reactions can occur. If less time is allowed for the inclusions to form, it only makes sense that there would be smaller inclusions and a smaller volume fraction. Another consideration is the time that larger inclusions are allowed to float out of the

weld pool and be trapped in the slag on top of the weld. This would tend toward larger inclusions trapped in the weld metal, which is not seen in any of the samples. Figure 4-8 shows that the mean inclusion diameter does in fact decrease with increasing cooling rate. Figure 4-9 shows that the inclusion volume fraction also decreases with increasing cooling rate. The scatter in these graphs can again be contributed to non-equilibrium conditions during welding. There is something else of interest in these two figures. The data is again segregated into regions associated with the HSLA-80 and HSLA-100 samples, but appears in this case to be associated with the cooling rate, which depends on the welding parameters and the plate thickness, not on the type of steel (HSLA-80 or HSLA-100). The fact that the cooling rate is higher for the HSLA-100 samples can be attributed to the thicker plate that was used as well as differences in the heat input. It is possible that these differences are responsible for the segregation between HSLA-80 and HSLA-100 data that was seen previously in Figures 4-4 through 4-6.

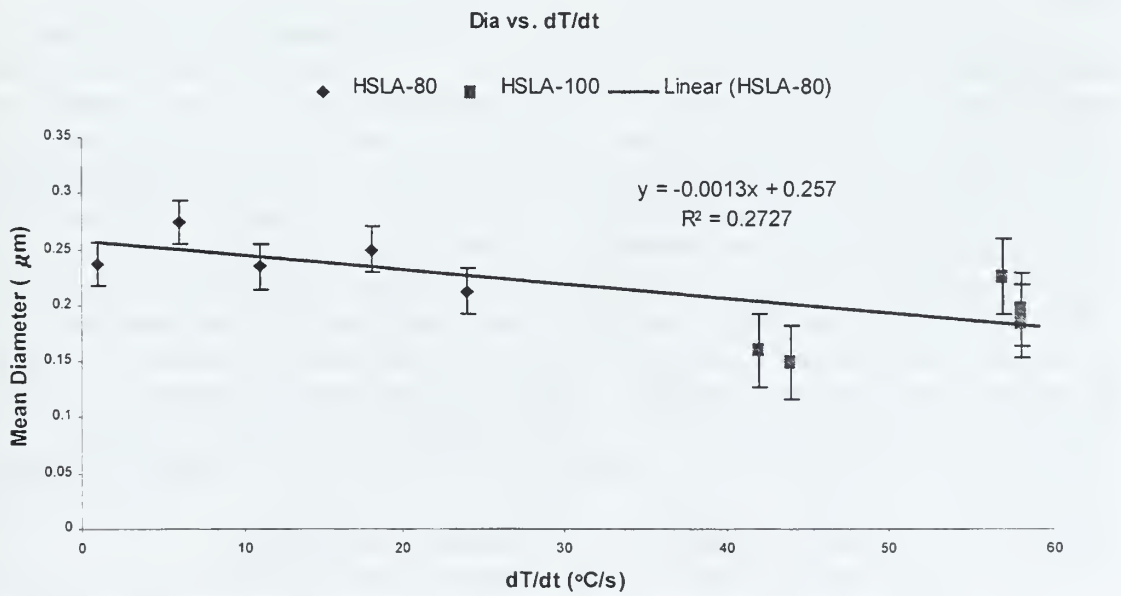

Figure 4-8: Non-metallic inclusion mean diameter vs. cooling rate.

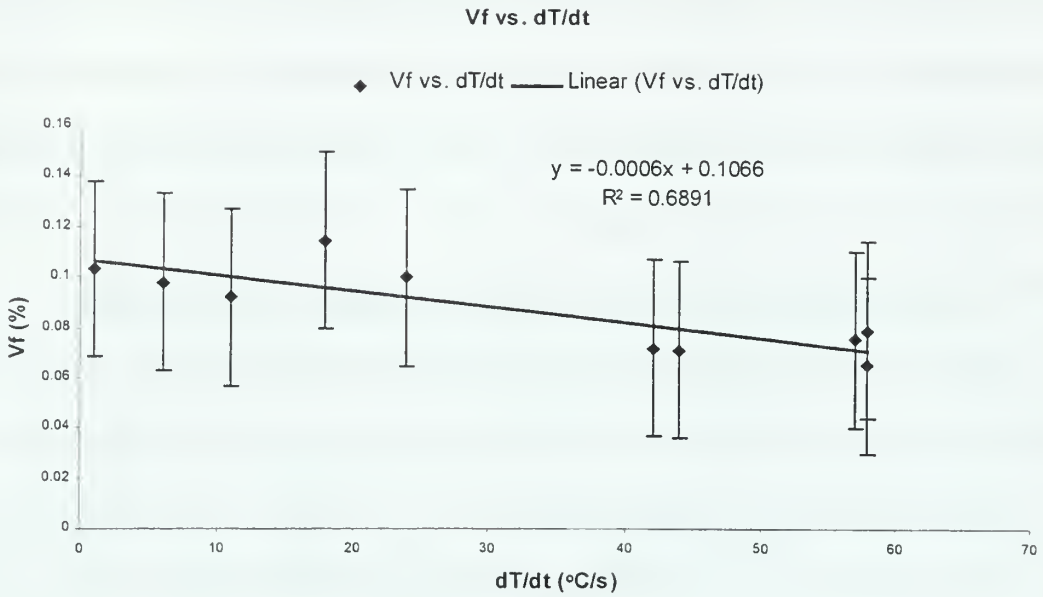

Figure 4-9: Non-metallic inclusion volume fraction vs. cooling rate.

2. Energy Dispersive X-Ray Analysis (EDX)

The non-metallic inclusion chemical compositions obtained by energy dispersive x-ray analysis were used to determine the relationship between inclusion chemistry and inclusion diameter and volume fraction in the weld metal. The most common elements found using EDX analysis were titanium, aluminum, silicon, manganese, oxygen, copper, sulfur, and iron. Iron was determined to have been lifted from the base metal along with the inclusion, and was not quantified. Copper was not quantified because the carbon extraction replica samples were on copper grids and sulfur was not quantified because it was seen in EDX spectrum imaging to only be present with the copper.

The relationships between weld metal titanium, aluminum, and silicon concentrations and the inclusion size and volume fraction have already been discussed.

Now, the relationships between the inclusion titanium, aluminum, and silicon concentrations and the inclusion size and volume fraction are addressed. The mean inclusion size appears to decrease with increasing titanium, but data scatter makes it difficult to say for sure. The volume fraction also decreases with increasing amounts of titanium in the inclusions. Figure 4-10 shows these trends. Trends with inclusion aluminum concentration could not be determined because of excessive data scatter. A decrease in inclusion size and volume fraction would be expected for increased amounts of deoxidation by stronger deoxidants [Ref. 13] Silicon has the opposite effect. The inclusion size and volume fraction both appear to increase with increasing silicon concentration in the inclusions. The manganese content of the inclusions also follows this trend, as expected. This trend is expected since the amount of silicon in the inclusion increases as the amounts of titanium and aluminum in the inclusions decrease (the total must equal 100%). Figure 4-11 shows these results.

Qualitative analysis was also performed using the EDX spectrum imaging technique as shown in Figure 3-15. The technique was used to gain understanding about where elements are concentrated in an inclusion, and is useful in predicting the possible compounds that are present in an inclusion. The EDX image in Figure 3-15 shows that copper and sulfur are found together (the bright patches show areas where the elements are, but the scattered areas indicate insignificant amounts of the elements in that area). This is probably in the form of copper-sulfide (CuS or Cu_2S), which forms as caps on inclusion surfaces. Manganese is essentially uniformly distributed throughout the inclusions, and since sulfur does not appear to be combined with the manganese, it exists as the oxide (MnO). Titanium does not occur in the same places in the sample as silicon

and aluminum, and aluminum and silicon do not appear where there is titanium. This has been seen in previous work as well, but recent research has also documented what is believed to be a compound consisting of titanium-oxide and alumina when deoxidation with manganese and silicon does not occur. [Ref. 13, 24]

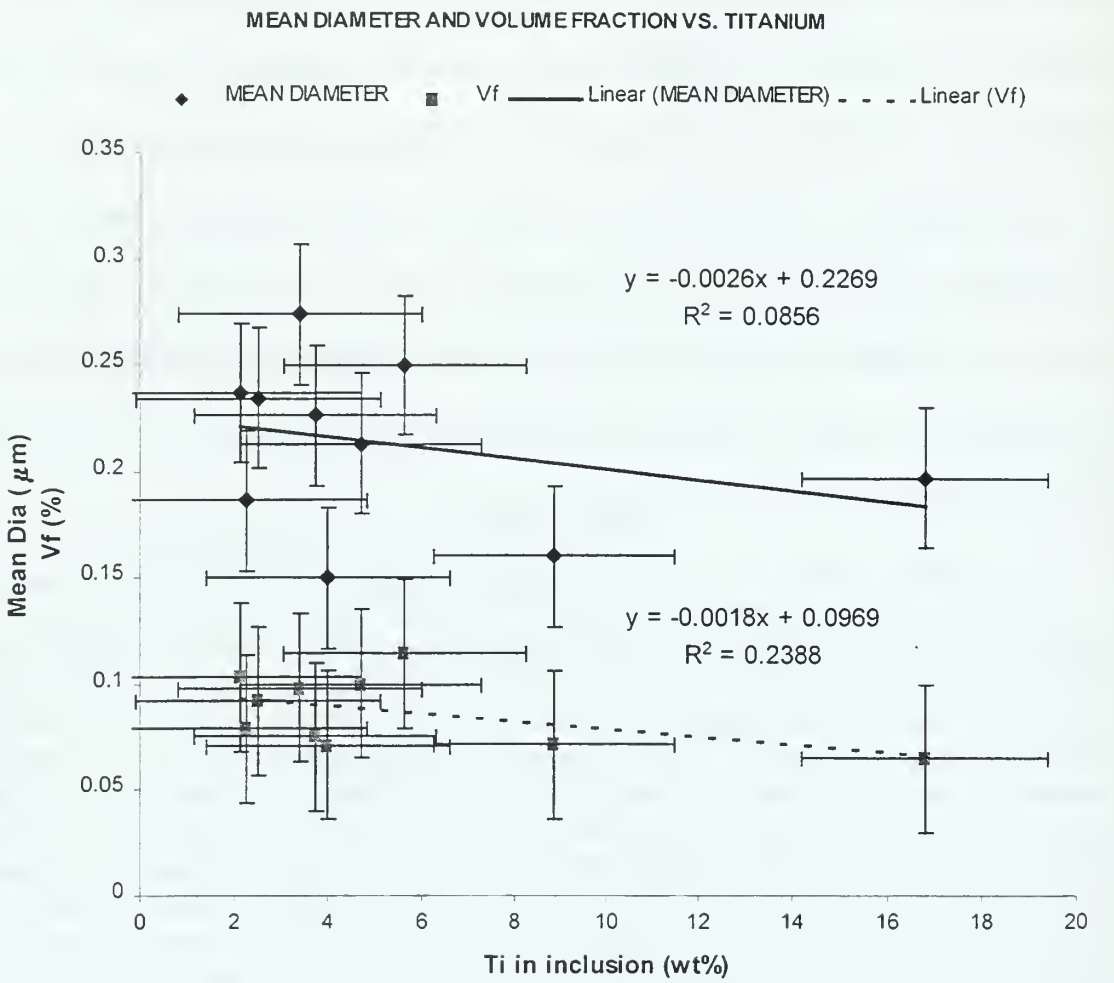

Figure 4-10: Inclusion mean diameter and volume fraction vs. inclusion titanium concentration.

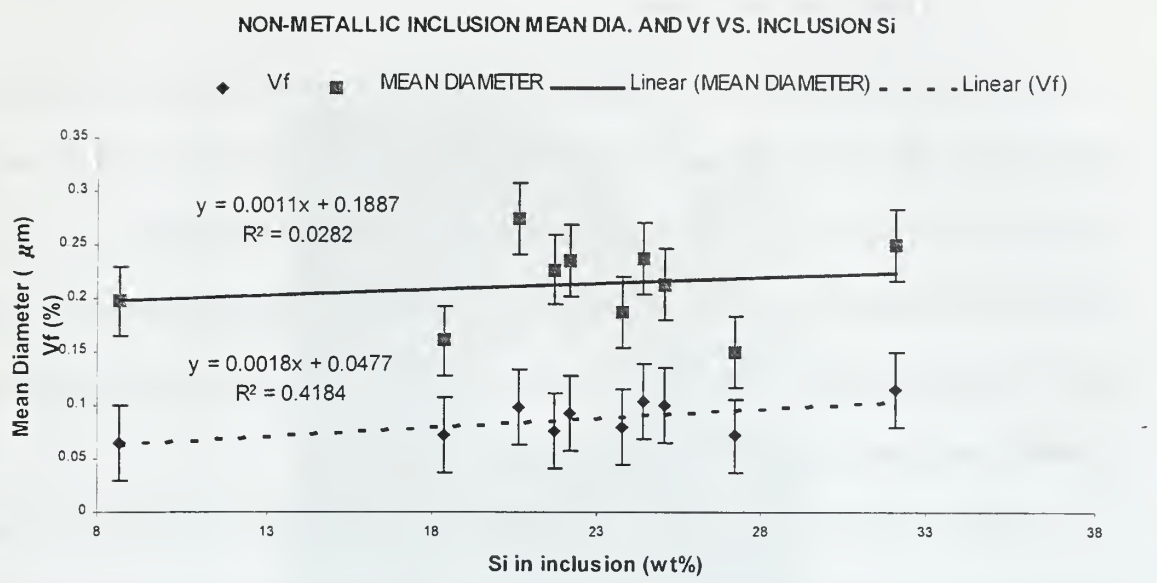

Figure 4-11: Inclusion mean diameter and volume fraction vs. inclusion silicon concentration.

The EDX spectrum imaging indicates that the inclusion is a multiphase particle, consisting primarily of two separate phases (not counting the CuS). The first phase, that contains titanium, manganese, and oxygen, is most likely a compound of titanium-oxide and manganese-oxide (TiO-MnO or TiO_2-MnO). The second phase appears to be a compound consisting of manganese-oxide, alumina, and silica (probably an Al_2O_3-MnO-SiO_2 ternary phase). Figure 3-15 is a typical representation of the phases and compounds that are present in all of the inclusions. The spectrum imaging also indicates that the titanium rich phase appears to be in the center of the inclusion, and is surrounded by the other phase. As already stated, the copper-sulfide usually forms caps on the surface of the inclusions.

3. TEM Thin Foil Sample

As stated in Chapter III, the purpose of analyzing a thin foil sample was to obtain micrographs of the typical microstructures present. The sample (PD 21092 S1) that was analyzed has a T_{50} of 470°C, which means that some martensite is expected. As was stated earlier, optical microscopy revealed mostly a granular ferritic microstructure with about 15% acicular ferrite. The thin foil sample was taken from an area that appears to be mostly martensite, with some acicular ferrite as well.

Figure 4-12 shows a STEM image of an inclusion with what appears to be acicular ferrite, surrounded by martensite (the ferrite plates are lighter than the martensite). Figure 4-13 shows a STEM image of lath ferrite and lath martensite. The ferrite is again the lighter area, while the martensite, which has a higher dislocation density, is the darker laths, and the dark regions between laths is retained austenite.

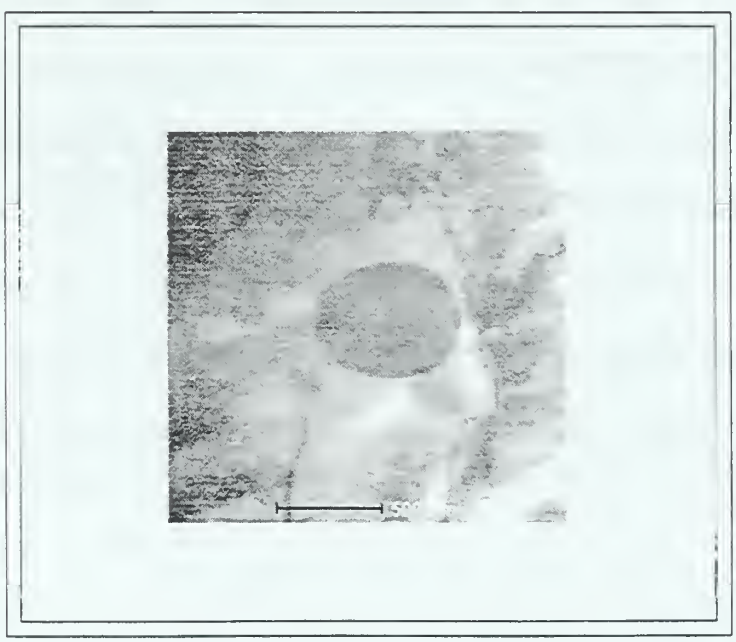

Figure 4-12: STEM image of an inclusion that nucleated acicular ferrite.

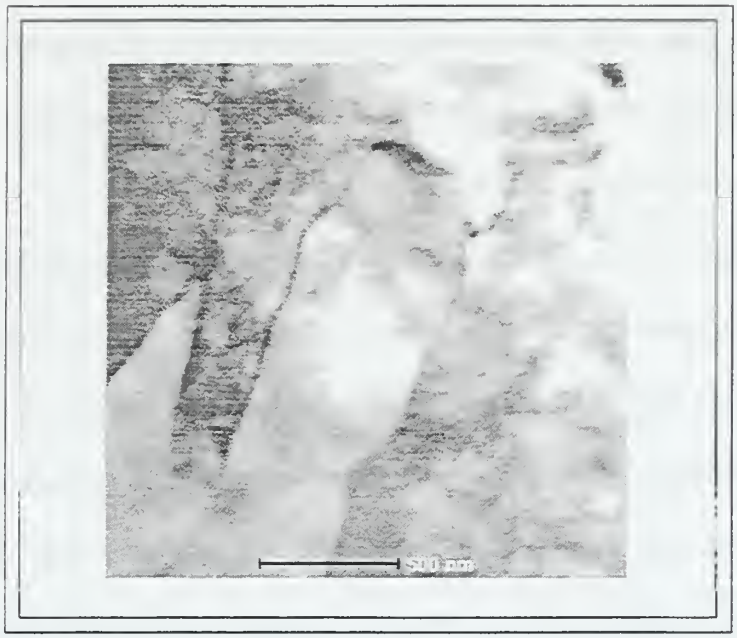

Figure 4-13: STEM image of martensite plates.

C. MECHANICAL PROPERTIES

It is extremely important to relate the microstructure and the non-metallic inclusion size and volume fraction to the strength and toughness of the weld metal. This is, in fact, the purpose of this research. The microstructure very simply relates to the strength and toughness of the weld. A finer microstructure should result in higher strength, and usually results in higher toughness, as well (the addition of alloying elements will lead to higher strength but lower toughness). This is why grain boundary ferrite has low strength and high toughness while martensite has high strength and low toughness. Figure 4-14 indicates that the strength is increased by increasing amounts of acicular ferrite and this increase is probably also reinforced by the fact that increasing

amounts of acicular ferrite results from increased cooling rates so that the overall microstructure is finer. The Charpy impact toughness of the samples appears unaffected by the acicular ferrite content and this is not surprising considering the small amounts of this finer microconstituent that is present in each one.

The strength and toughness are also likely to be affected by the non-metallic inclusion mean diameter and volume fraction. The strength should increase with increasing inclusion size and with increasing inclusion volume fraction. This, however, is not observed directly. Figure 4-15 indicates that strength decreases with increasing inclusion diameter and Figure 4-16 shows that strength decreases with increasing inclusion volume fraction. The fact that the strength is not increasing with increasing levels of inclusions is believed to be due to the alloying content and thus the microstructure. The microstructure, as already stated, goes from coarse polygonal ferrite to fine martensite as T_{50} decreases. Figure 4-17 indicates that the inclusion size and volume fraction decrease as T_{50} decreases, and is due to decreasing cooling rate (equation 4-1). Therefore, the matrix microstructure appears to have a more dominant effect on strength than the inclusion size and volume fraction.

The non-metallic inclusion diameter and volume fraction both decrease with increasing cooling rate (Figures 4-8 and 4-9). The strength decreases with increasing inclusion size and volume fraction. These two trends indicate that the strength should increase with increasing cooling rate. This is seen to be true in Figure 4-18. Figure 4-18 also show that cooling rate has no affect on the toughness.

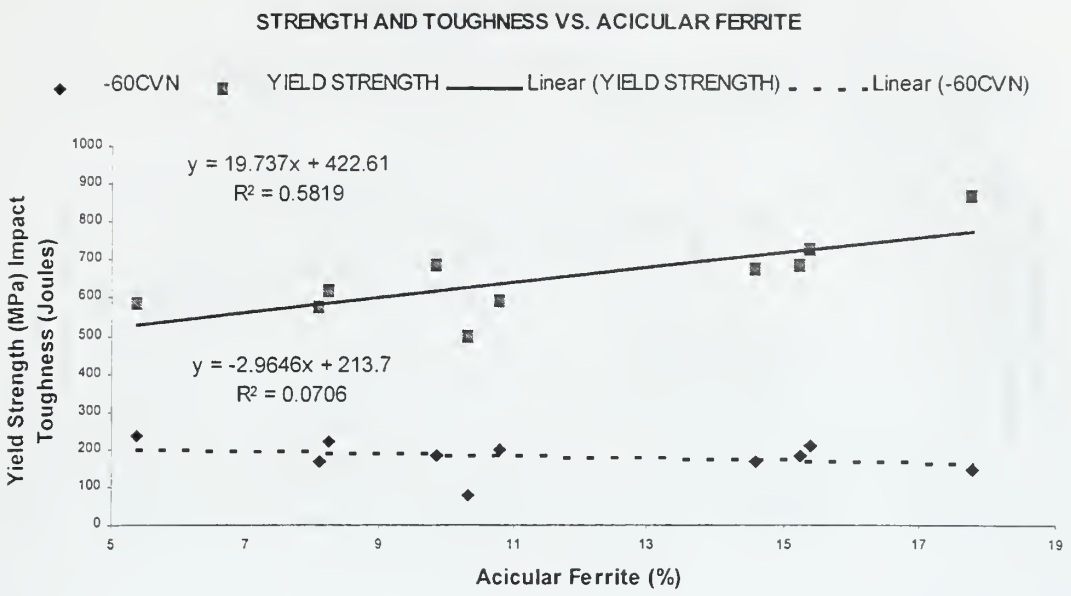

Figure 4-14: Strength and toughness vs. amount of acicular ferrite.

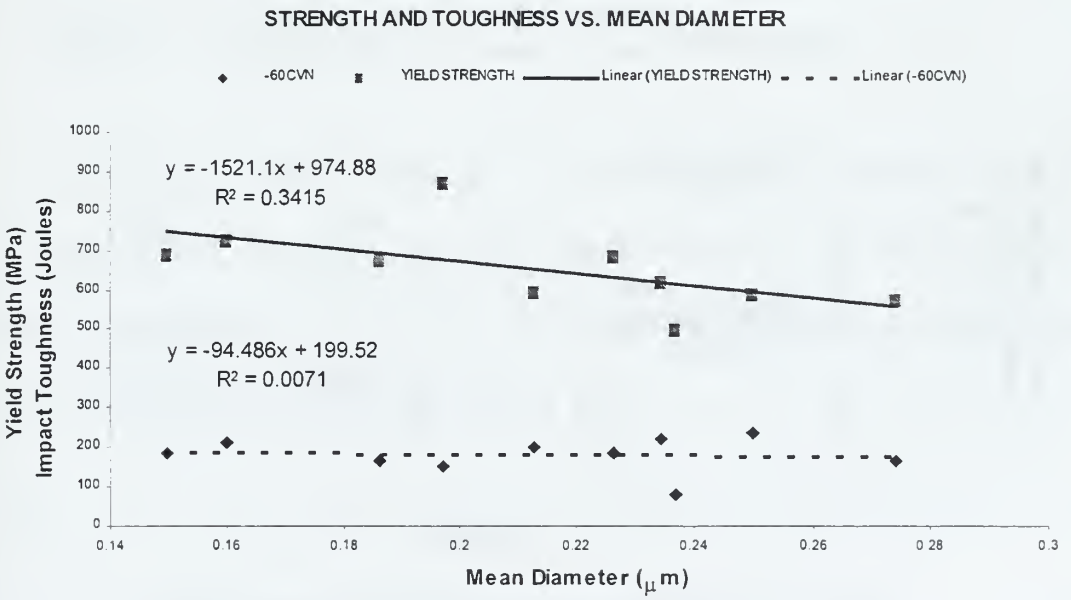

Figure 4-15: Strength and toughness vs. inclusion mean diameter.

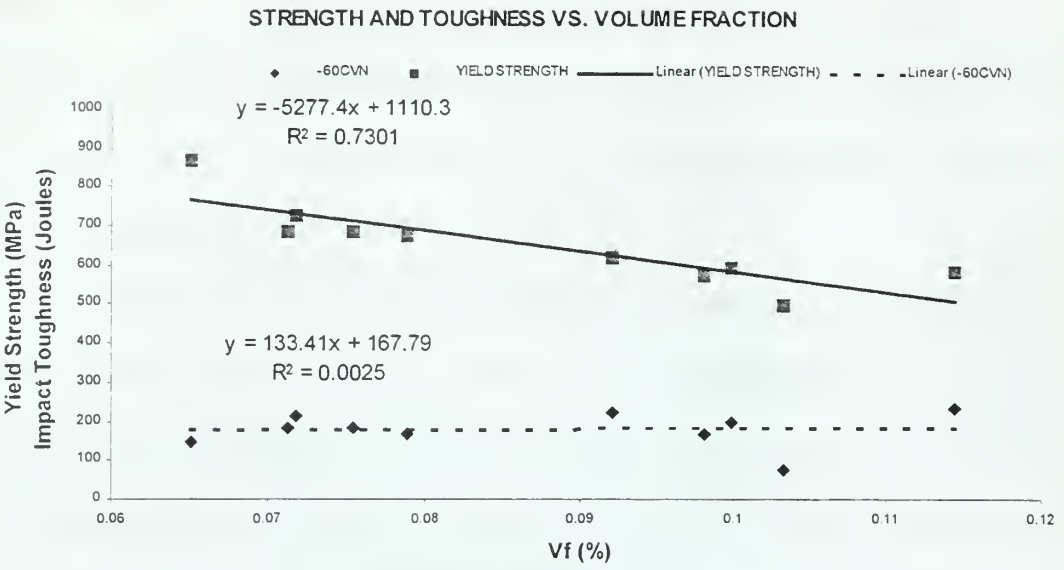

Figure 4-16: Strength and toughness vs. inclusion volume fraction.

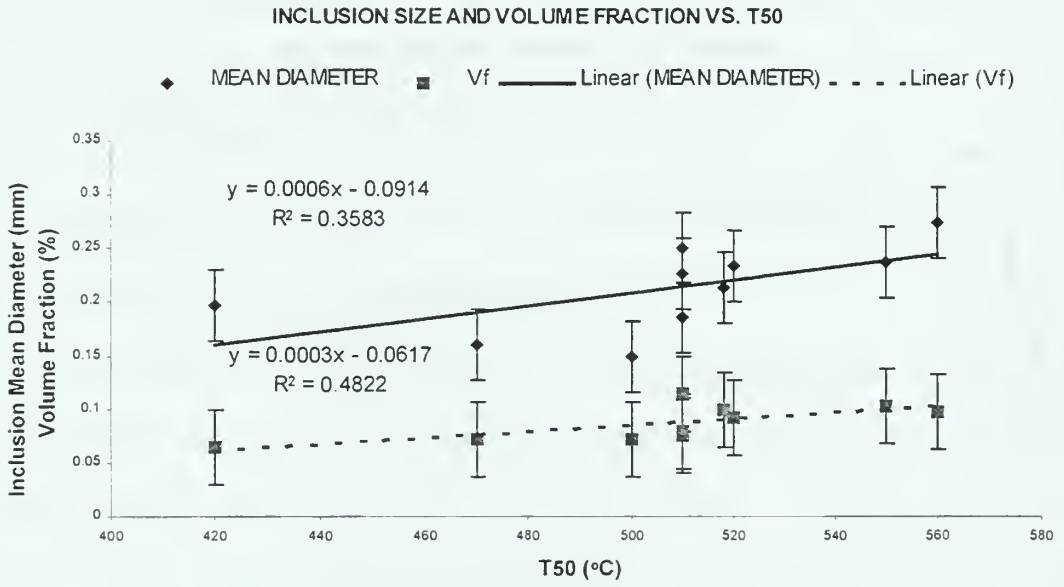

Figure 4-17: Inclusion size and volume fraction vs. T50.

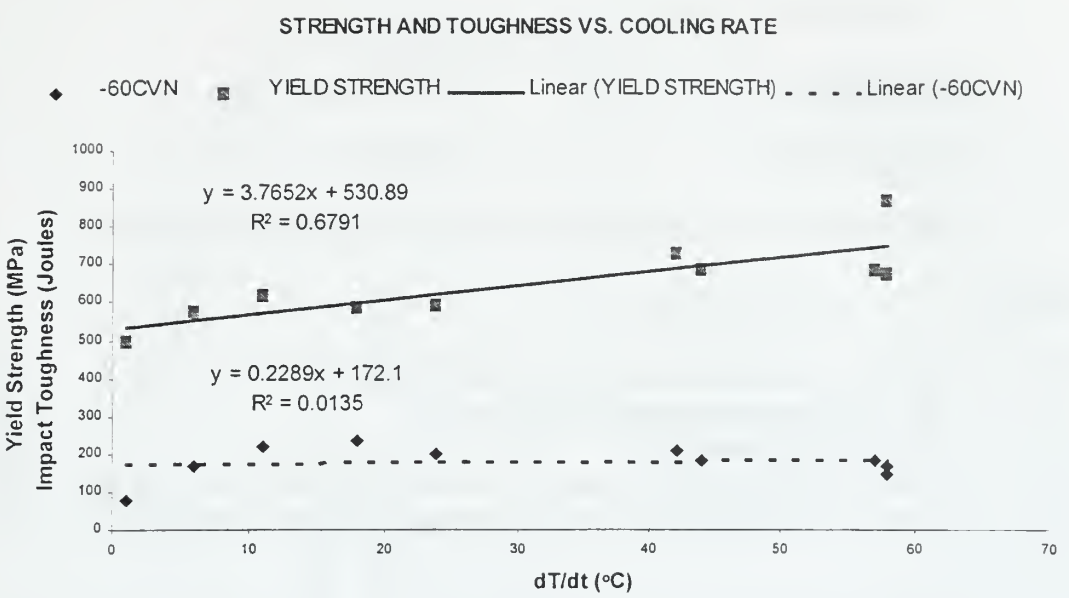

Figure 4-18: Strength and toughness vs. cooling rate.

D. MODELS OF MECHANICAL PROPERTIES

Joe Blackburn, NSWC Carderock Division, used regression statistics to model the 50% transformation temperature, the prior austenite grain size, the yield strength, the ultimate tensile strength, and the –60 C Charpy impact toughness. [Ref. 15] Equations 4.1 through 4.7 are the results of the modeling.

$$T_{50}=780-13\ln(dT/dt)-1266C-56Mo-45Ni-3.6(Si/O) \quad (4.1)$$

$$\gamma_{gw}=31+6872(O) \qquad T_{50}>510°C \quad (4.2)$$

$$\gamma_{gw}=241+15(Ni)^2-434(Mo) \qquad T_{50}\leq 510°C \quad (4.3)$$

$$\sigma_y = 1297 + 14z - 1.2T_{50} - 0.48\dot{\gamma}_{gw} \quad (4.4)$$

$$\sigma_{uts} = 1332 - 1.38T_{50} + 61CdT/dt \qquad T_{50} > 510°C \quad (4.5)$$

$$\sigma_{uts} = 890 - 0.48T_{50} \qquad T_{50} \leq 510°C \quad (4.6)$$

$$\ln(CVN) = -0.16z + 0.47\ln(dT/dt) + 3.8(\sigma_y/\sigma_{uts}) + 0.06(Si/O) - 0.45(CdT/dt) \quad (4.7)$$

where,

dT/dt = calculated cooling rate at 538°C (°C/s)
T_{50} = 50% transformation temperature (°C)
z = plate thickness (cm)
C, Mo, Ni, O = concentrations of associated elements in weld metal (wt%)
σ_y , σ_{uts} = 2% offset yield strength, ultimate tensile strength (Mpa)

It is easy to explain the factors affecting the T_{50}. The cooling rate has a negative effect in that as the cooling rate increases, the transformation from austenite to the lower temperature microstructure is suppressed, and the T_{50} decreases. Increasing the alloy content and/or decreasing the oxygen forces the curves of Figure 4-2 to the right, which also suppresses the T_{50}. The dT/dt and the Si/O terms both include the effect of non-metallic inclusions. The size and volume fraction of inclusions decrease as cooling rate increases (Figures 4-8 and 4-9). The size and volume fraction of inclusions also decrease as the ratio of silicon content to oxygen content in the weld metal increases (Figure 4-19). Both of these factors should result in decreasing the T_{50} when inclusion size and/or volume fraction are increased. Figure 4-17 indicates that the opposite trends may occur, but it is difficult to be sure as the error bars are somewhat large.

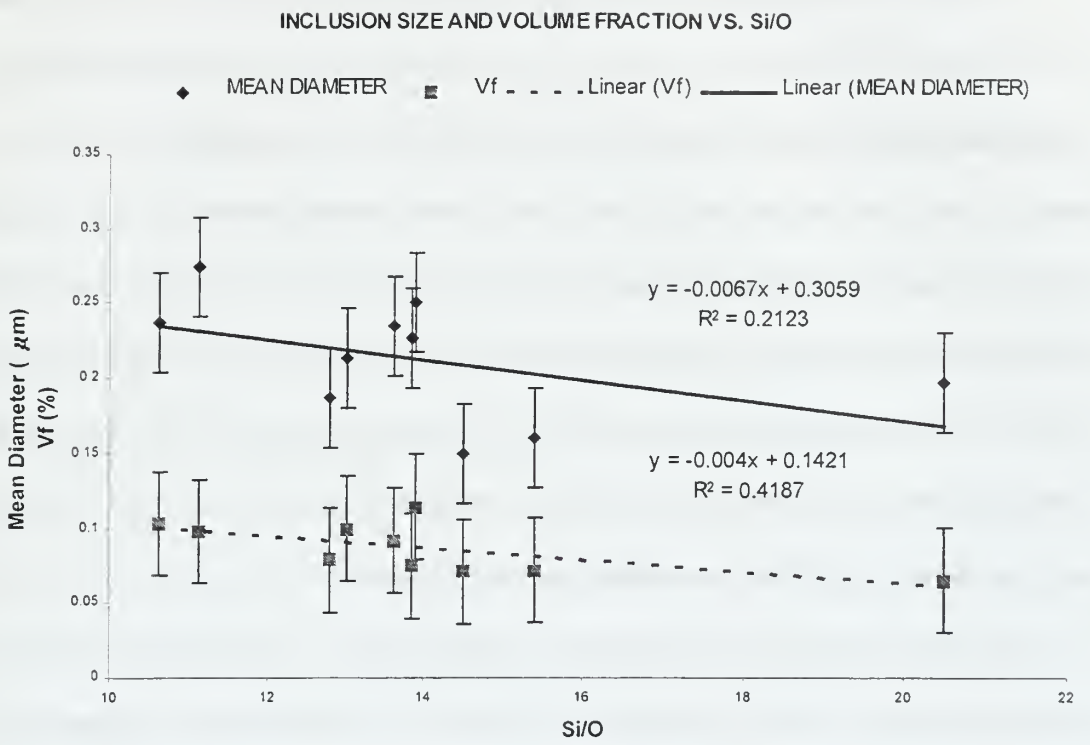

Figure 4-19: Non-metallic inclusion size and volume fraction vs. weld metal silicon to oxygen ratio

It is apparent that silicon content is more significant than aluminum or titanium in this model, but aluminum and titanium are stronger deoxidizers than silicon. One possible explanation for the significance of silicon is that it is present in significantly higher percentages than aluminum and titanium. Therefore, the oxygen reacts with the two strongest deoxidants, aluminum and titanium, and there is sufficient excess oxygen in the weld metal to react with the silicon and manganese. EDX analysis showed that, in general, there is significantly more silicon than titanium or aluminum in most of the non-metallic inclusions. Therefore it is the absence of titanium and aluminum that may make the silicon (and manganese) appear as more dominant deoxidants.

The prior austenite grain width model will not be discussed in detail in this study, since it does not affect the current results, is not required to explain the other models, and is explained in the technical report by Blackburn. [Ref. 15] One thing will be mentioned, though. Two equations are required to capture the nature of grain width. One of these equations is dependent only on oxygen content, and is valid if T_{50} is greater than 510°C, and the other depends on nickel and molybdenum and is valid for T_{50} less than or equal to 510°C. This separation can be correlated with the microstructure, since it was determined that for the latter case, significant martensite is present, but for the former case, there is not a significant amount of martensite present.

The yield strength model depends on plate thickness, T_{50}, and grain width. It is obvious that larger grains lower strength. The plate thickness and the cooling rate (in the T_{50} term) may be an indication of a dependence of the yield strength on the heat input, weld bead size, or degree of reheating. The effect of T_{50} on the yield strength includes another component of cooling rate, and also includes the effect of alloying. As the cooling rate increases, it is again obvious that the strength should increase as well (Figure 4-17). This is the result of a finer microstructure. The affect of the alloying agents here is the same as that described for the T_{50} model. Notice that the yield strength model is independent of the presence of martensite. However, this is not the case with the ultimate tensile strength.

The ultimate tensile strength model (equations 4-5 and 4-6), as with the grain width model, depends on the presence of martensite. Two equations are required, and the validity of each equation changes at 510°C. The model for $T_{50} \leq 510$°C is dependent on the T_{50}, carbon content, and cooling rate. The model for $T_{50} > 510$°C depends on just the

T_{50}. Again, this can be attributed to the formation of significant amounts of martensite for the $T_{50} \leq 510°C$.

The final model to consider is that for toughness. This model predicts the Charpy impact energy at a test temperature of –51C (-60F), and is dependent on the plate thickness, cooling rate, ratio of yield and ultimate tensile strengths, the ratio of silicon to oxygen, and the product of carbon content and cooling rate. All of the terms occur here for the same reasons that they occur in the other models except one. This is the only model that has the strength ratio term in it. Figure 4-20 shows that the strength ratio increases with increasing yield strength, but it appears to level off at about 0.95 and yield strength of about 680 MPa. This indicates that the toughness increases with increasing yield strength, at least initially. This does not appear to be the result of a finer microstructure since the T_{50}, which is a good indicator of the fineness of the microstructure, does not appear to have an affect on the toughness (Figures 4-21).

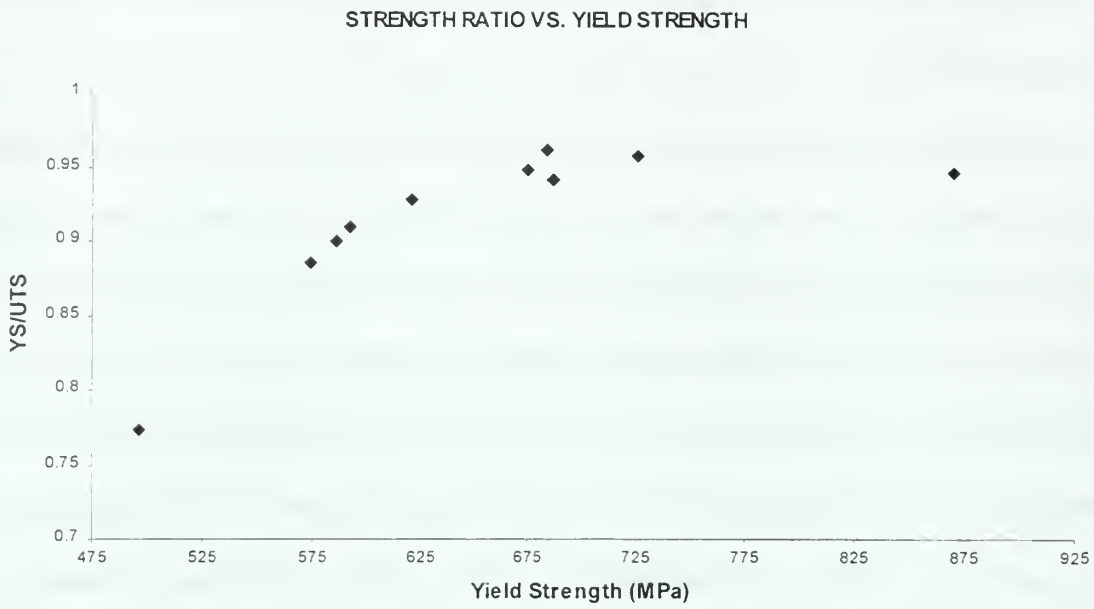

Figure 4-20: Strength ratio vs. yield strength

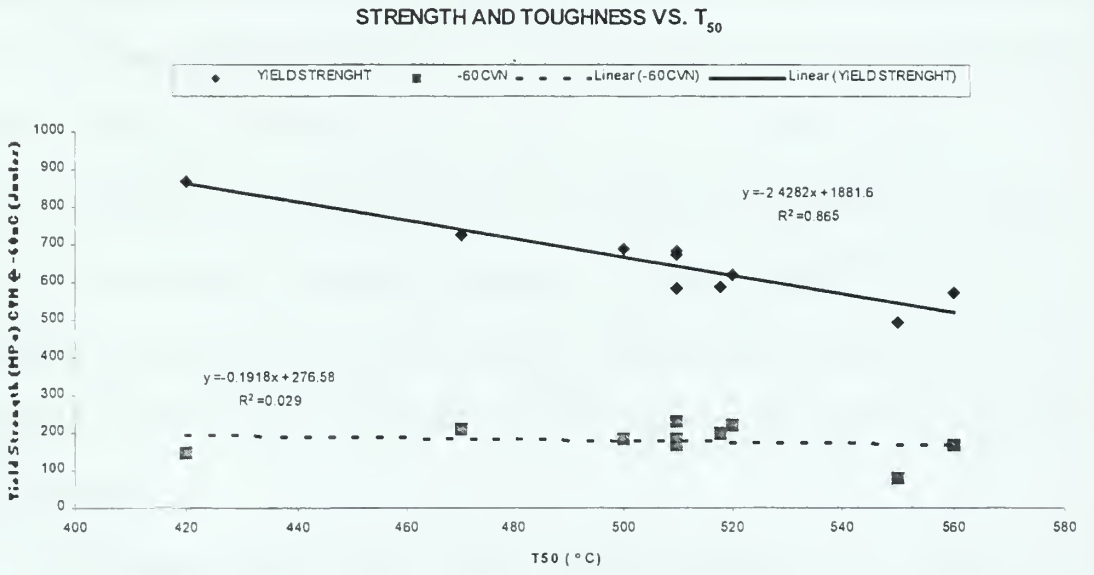

Figure 4-21: Strength and toughness vs. T_{50}.

V. SUMMARY

A. CONCLUSIONS

The weld metal microstructures of all of the weld samples consisted primarily of granular ferrite, with varying amounts of polygonal ferrite, acicular ferrite, and martensite. Although acicular ferrite is the desired weld metal microstructure, it is difficult to get significant amounts in ultra-low carbon steel welds using the GMAW process and ultra-low carbon consumables. Even with low amounts of acicular ferrite, though, all of the samples except one (PD 21150) met the strength and toughness requirements of MIL-100S. The one sample that failed to meet the required strength appeared to do so mainly due to the welding parameters (slow cooling rate), which resulted in large grains and a large amount of polygonal ferrite. This sample also had the highest weld metal oxygen content, which resulted in larger inclusions and a higher volume fraction of inclusions

The 50% transformation temperature has been found to be a good indicator of the transition of the microstructure from polygonal ferrite to martensite, and therefore also a good indicator of strength. [Ref. 15] The 50% transformation temperature can also be used to estimate the amount of acicular ferrite present (see Figure 4-1).

It is desired to minimize the size and volume fraction of non-metallic inclusions if they do not appear to nucleate significant amounts if acicular ferrite. Non-metallic inclusion size and volume fraction depend on oxygen, titanium, aluminum and silicon concentrations in the weld metal, and titanium and silicon concentrations in the

inclusions. As the oxygen concentration in the weld metal increases, the mean inclusion diameter and volume fraction both increase. As the titanium and aluminum concentrations in the weld metal increase, the inclusion volume fraction decreases, and the mean inclusion diameter decreases to a minimum (at Ti + Al $\approx$ 0.011 wt%) and then starts to increase again. The inclusion size and volume fraction both decrease with increasing silicon concentration in the weld metal. The mean inclusion diameter and the volume fraction of inclusions also decrease as the titanium concentration in the inclusion increases (or as the silicon concentration in the inclusion decreases).

The inclusion size and volume fraction are also dependent on the cooling rate. As the cooling rate increases, both the mean inclusion diameter and the volume fraction of inclusions decrease.

Most of the inclusions were multiphase particles consisting of two primary phases. The first phase consists of manganese-oxide and titanium-oxide. The second phase, which appears to form around the first, consists of manganese-oxide, silica, and alumina. Copper-sulfide caps were also found on the surfaces of some inclusions.

B. SUGGESTIONS FOR FURTHER STUDY

It appears that ultra-low consumables have been developed that meet the weld strength and toughness requirements of MIL-100S when used to weld HSLA-80 and HSLA-100 steel plates with out the need for preheat or interpass temperature controls.

Fifty-two weld samples have been analyzed for microstructure and mechanical properties, but only a fraction of them have been analyzed for non-metallic inclusions. Additional research is required to validate the effect of welding parameters and weld metal chemistry on the formation of non-metallic inclusions, and on how the inclusions affect the mechanical properties. More data is also required to develop more accurate statistical models for predicting the size and volume fraction of inclusions and to correlate these models with the models presented by NSWC.

LIST OF REFERENCES

1. Kou, S., *Welding Metallurgy*, John Wiley & Sons, Inc., New York, 1987.

2. Reck, V., Jr., *Mechanical and Microstructural Properties of Ultra-Low Carbon Bainitic Steel Weld Metal*, Masters Thesis, Naval Postgraduate School, Monterey, CA, 1995.

3. Department of the Navy Military Specification MIL-E-23765/2E(SH), *Electrodes and Rods-Welding, Bare, Solid, or Alloy Cored; and Fluxes, Low Alloy Steel*, 22 April, 1994.

4. Holsberg, P., Gudas, J., and Caplan, I., "Metallurgical Design and Processes in the U.S. Navy High Strength Steel Welding," *Recent Trends in Welding Science and Technology*, 1989.

5. Grong, O. and Matlock, D.K., "Microstructural Development in Mild and Low-Alloy Steel Weld Metals," *International Metals Reviews*, v. 31, 1986.

6. Gwin, M.E., *Factors Affecting the Impact Toughness of Ultra Low Carbon Steel Weld Metal*, Masters Thesis, Naval Postgraduate School, Monterey, CA, 1996.

7. Brumbaugh, J.E., *Welders Guide*, Macmillan Publishing Company, 1986.

8. *Guidelines for Classification of Ferritic Steel Weld Metal Microstructure Constituents using the Light Microscope*. IIW Doc. No. IXJ-102-85.

9. Thompson, S.W., Colvin, D.J., and Krauss, G., "Continuous Cooling Transformations and Microstructures in a Low-Carbon, High-Strength Low-Alloy Plate Steel," *Metallurgical Transactions A*, Vol. 21A, June 1990.

10. Shewmon, P.G., *Transformations in Metals*, J. Williams Book Company, Jenks, OK, 1983.

11. Lui, S., "Metallography of HSLA Steel Weldments," *Key Engineering Materials*, Vol. 69-70, 1992.

12. Bhadeshia, H.K.D.H., *Bainite in Steels*, Institute of Materials, London, Chapter 10, 1990.

13. Mahony, Michael F., *Investigation into the Mechanism of Acicular Ferrite Nucleation in Steel Weld Metal*, Masters Thesis, Naval Postgraduate School, Monterey, CA, 1999.

14. Porter, David A. and Easterling, Kenneth E., *Phase Transformations in Metals and Alloys*, Van Nostrand Reinhold Company, New York, 1988.

15. Blackburn, J.M., *Factors Affecting the Strength and Toughness of Low Carbon Alloy Steel Weld Metals*, Survivability, Structures, and Materials Directorate Technical Report, NSWCCD-TR-61-98/33, November, 1998.

16. Williams, David B. and Carter, C.B., *Transmission Electron Microscopy*, Vol 1, Plenum Press, New York, 1996.

17. ASTM Standard E 562-89, "Standard Test Method for Determining Volume Fraction by Systematic Manual Point Count," *Annual Book of ASTM Standards*, 1995.

18. Gladman, T. and Woodhead, J.H., "The Accuracy of Point Counting in Metallographic Investigations", *Journal of the Iron and Steel Institute*, February, 1960.

19. Smallman, R.E., *Modern Physical Metallurgy*, Butterworth-Heinemann Ltd., Oxford, 1992.

20. DeHoff, R.T. and Rhines, F.N., *Quantitative Microscopy*, McGraw-Hill, Inc., 1989.

21. Topcon Corporation, "New Analytical Ultra-High Resolution EM-002B 200kV," Advertisement Brochure printed in Japan.

22. Beckwith, T.G., Lienhard V, J.H.. and Marangoni, R.D., *Mechanical Measurements*, Addison-Wesley Publishing Company, Fifth Edition, 1995.

23. Blackburn, J.M., Fox, A., and Vassilaros, M., "Factors Affecting Impact Toughness of Low Carbon Bainitic Weld Metal," Paper Presented Fourth International Conference of Trends in Welding Research, Gatlinburg, TN, June 1995.

24. Fox, A.G., Private Communications, 1998.

APPENDIX A. CHARACTERISTICS OF WELD SAMPLES

WELD ID		PD 21092 S1	PD 21092 S2	PD 21149	PD 21150
PROCESS		GMAW-P	GMAW-P	GMAW-S	GMAW-S
POSITION		VERT	VERT	FLAT	FLAT
PLATE		HSLA-100	HSLA-100	HSLA-80	HSLA-80
THICKNESS	cm	5.08	5.08	1.91	0.95
WIRE ID		ARC-100N	ARC-100N	ARC-100N	ARC-100N
dT/dt	°C	42	44	11	1
YS	Mpa	726	687	620	496
UTS	Mpa	758	730	668	641
EL	%	22	22	25	26
RA	%	76	76	77	76
CVN @ 0°F	Joules	245	229	256	130
CVN @ -60°F	Joules	211	184	221	78
T_{50}	°C	470	500	520	550
C	wt%	0.026	0.028	0.049	0.037
Mn	wt%	1.52	1.52	1.27	1.28
Si	wt%	0.28	0.29	0.29	0.29
Cr	wt%	0.04	0.04	0.15	0.15
Ni	wt%	2.71	2.71	2.29	2.12
Mo	wt%	0.48	0.47	0.45	0.43
Cu	wt%	0.075	0.108	0.13	0.13
S	wt%	0.001	0.001	0.003	0.005
P	wt%	0.002	0.003	0.003	0.003
Al	wt%	0.002	0.003	0.011	0.002
Ti	wt%	0.005	0.005	0.004	0.004
O	wt%	0.0182	0.02	0.0213	0.0273
N	wt%	0.0032	0.0013	0.0058	0.0032
γGS	μm	NO DATA	134	119	229
INCL MEAN DIA	μm	0.165988	0.154436	0.240403	0.252872
INCL DIA STDEV	μm	0.04521	0.039257	0.077557	0.083637
INCL Vf	%	0.0718	0.0713	0.0921	0.1033
INCL Vf STDEV	%	0.1093	0.0405	0.1829	0.0807
Ti + Al	%	0.007	0.008	0.015	0.006

WELD ID		PD 21151	PD 21151 S2	PD 21176	PD 21242
PROCESS		GMAW-S	GMAW-S	GMAW-S	GMAW-S
POSITION		FLAT	FLAT	FLAT	FLAT
PLATE		HSLA-100	HSLA-100	HSLA-80	HSLA-80
THICKNESS	cm	5.08	5.08	0.95	2.54
WIRE ID		ARC-100N	ARC-100N	ARC-100N	ARC-100N
dT/dt	°C	57	58	6	24
YS	Mpa	684	675	574	592
UTS	Mpa	712	712	648	651
EL	%	22	22	27	24
RA	%	73	74	81	76
CVN @ 0°F	Joules	224	234	203	235
CVN @ -60°F	Joules	185	166	167	199
T_{50}	°C	510	510	560	518
C	wt%	0.022	0.022	0.044	0.027
Mn	wt%	1.4	1.41	1.28	1.35
Si	wt%	0.27	0.27	0.26	0.25
Cr	wt%	0.04	0.03	0.14	0.07
Ni	wt%	2.7	2.72	2.36	2.45
Mo	wt%	0.47	0.5	0.46	0.47
Cu	wt%	0.078	0.091	0.235	0.111
S	wt%	0.001	0.001	0.002	0.003
P	wt%	0.003	0.002	0.003	0.002
Al	wt%	0.003	0.002	0.001	0.005
Ti	wt%	0.004	0.004	0.004	0.003
O	wt%	0.0195	0.0211	0.0234	0.0192
N	wt%	0.0018	0.0023	0.0034	0.0011
γGS	μm	148	149	192	183
INCL MEAN DIA	μm	0.239551	0.196269	0.272689	0.22503
INCL DIA STDEV	μm	0.105286	0.044931	0.082149	0.062667
INCL Vf	%	0.0754	0.0789	0.0981	0.0999
INCL Vf STDEV	%	0.048	0.0571	0.0789	0.0538
Ti + Al	%	0.007	0.006	0.005	0.008

WELD ID		PD 21251 S2	PD 21255
PROCESS		GMAW-S	GMAW-S
POSITION		FLAT	FLAT
PLATE		HSLA-100	HSLA-80
THICKNESS	cm	5.08	1.91
WIRE ID		ARC-100R	ARC-100N
dT/dt	°C	58	18
YS	Mpa	870	586
UTS	Mpa	919	651
EL	%	18	24
RA	%	68	77
CVN @ 0°F	Joules	182	265
CVN @ -60°F	Joules	149	234
T_{50}	°C	420	510
C	wt%	0.043	0.025
Mn	wt%	1.63	1.38
Si	wt%	0.32	0.26
Cr	wt%	0.03	0.03
Ni	wt%	3.08	2.54
Mo	wt%	0.69	0.48
Cu	wt%	0.146	0.081
S	wt%	0.002	0.002
P	wt%	0.003	0.001
Al	wt%	0.006	0.001
Ti	wt%	0.01	0.003
O	wt%	0.0156	0.0187
N	wt%	0.0022	0.0011
γGS	µm	94	147
INCL MEAN DIA	µm	0.202855	0.253091
INCL DIA STDEV	µm	0.056841	0.067752
INCL Vf	%	0.0651	0.1145
INCL Vf STDEV	%	0.0546	0.0644
Ti + Al	%	0.016	0.004

APPENDIX B. NON-METALLIC INCLUSION SIZE DISTRIBUTION

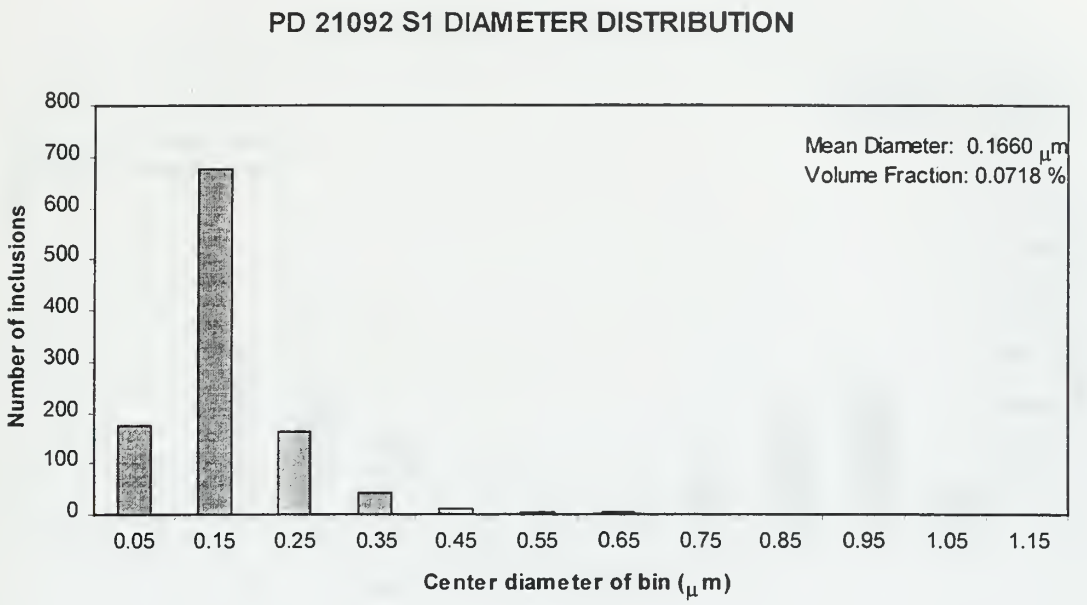

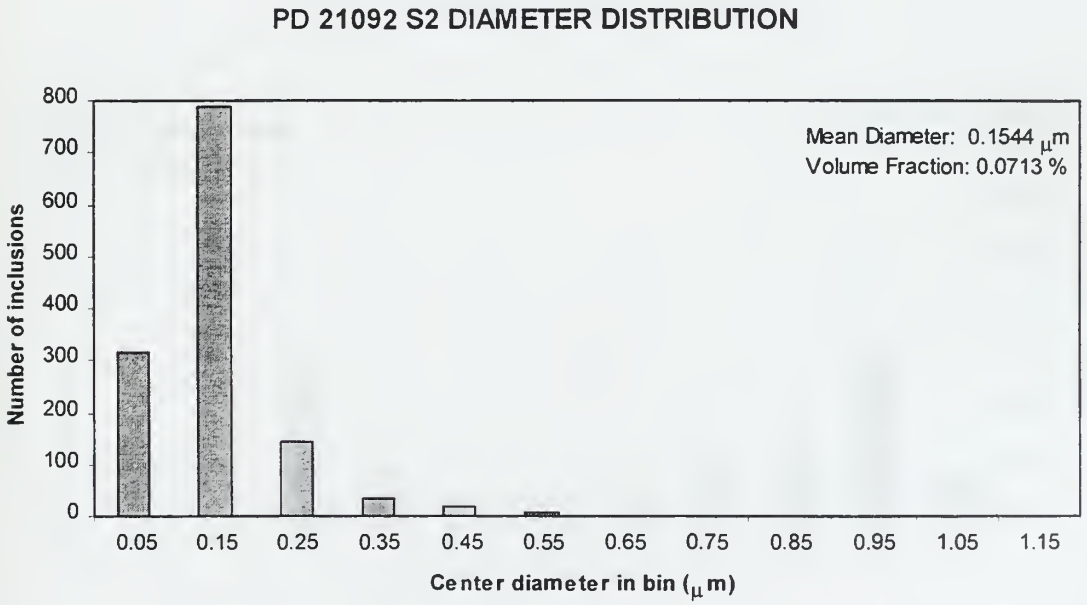

PD 21149 DIAMETER DISTRIBUTION

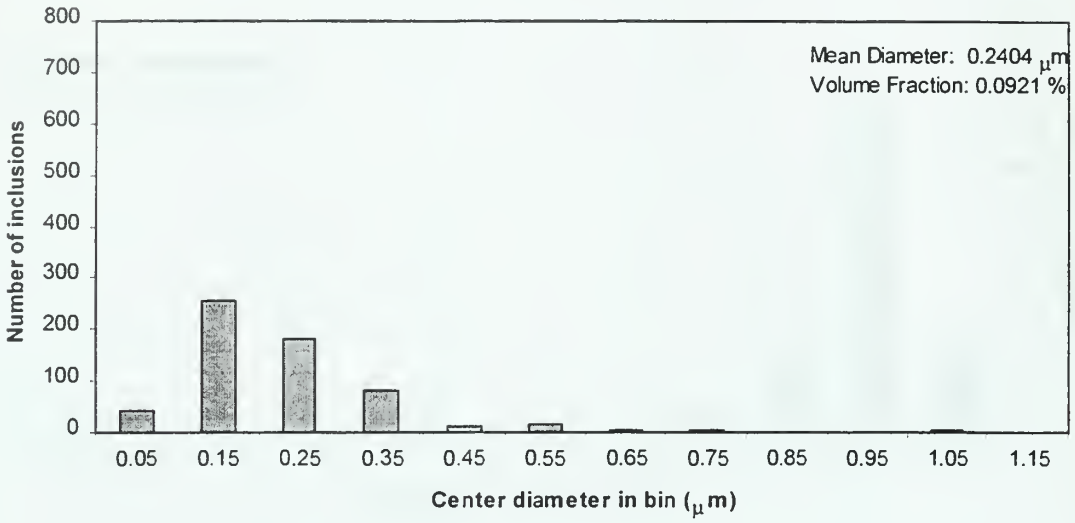

PD 21150 DIAMETER DISTRIBUTION

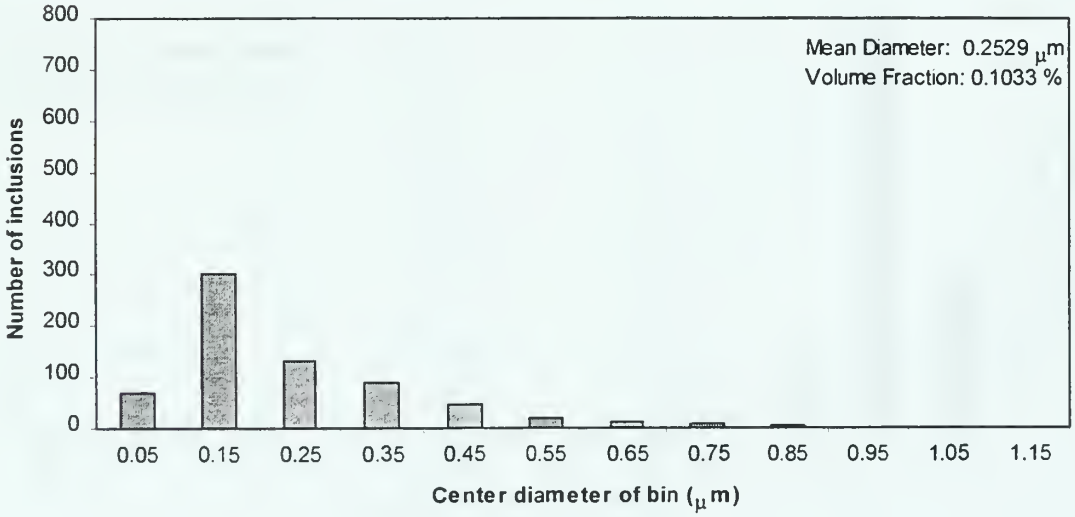

PD 21151 DIAMETER DISTRIBUTION

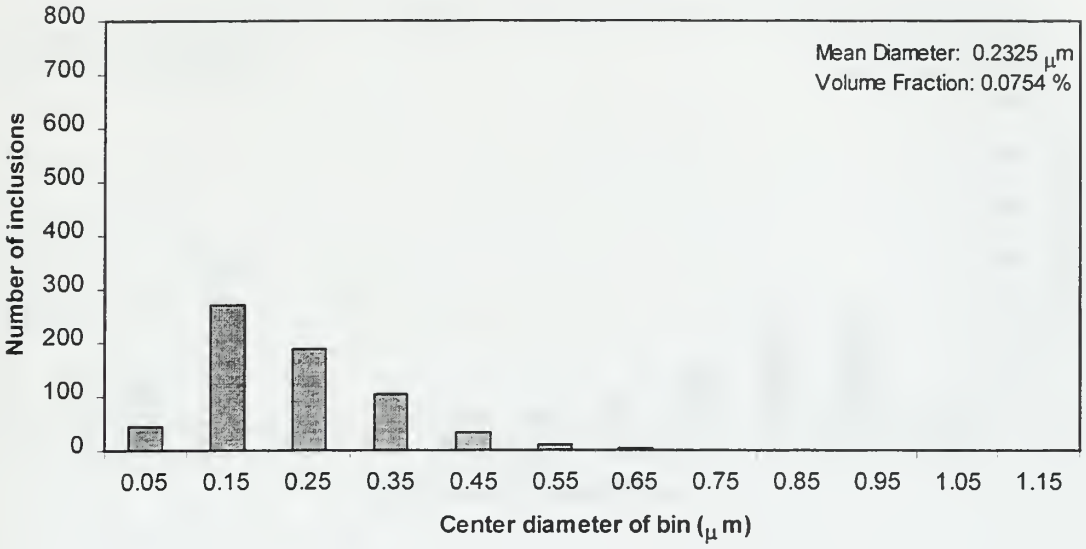

PD 21151 S2 DIAMETER DISTRIBUTION

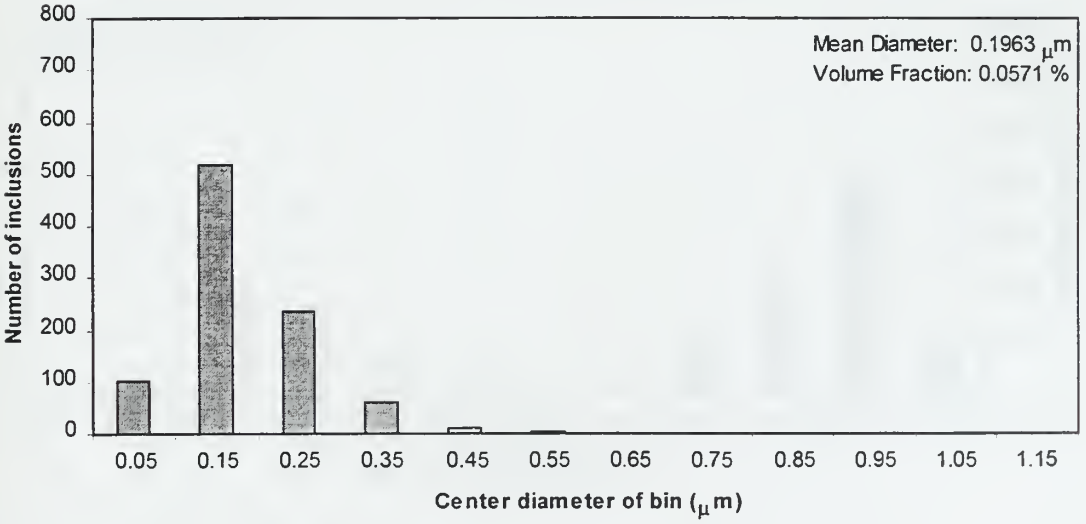

PD 21176 DIAMETER DISTRIBUTION

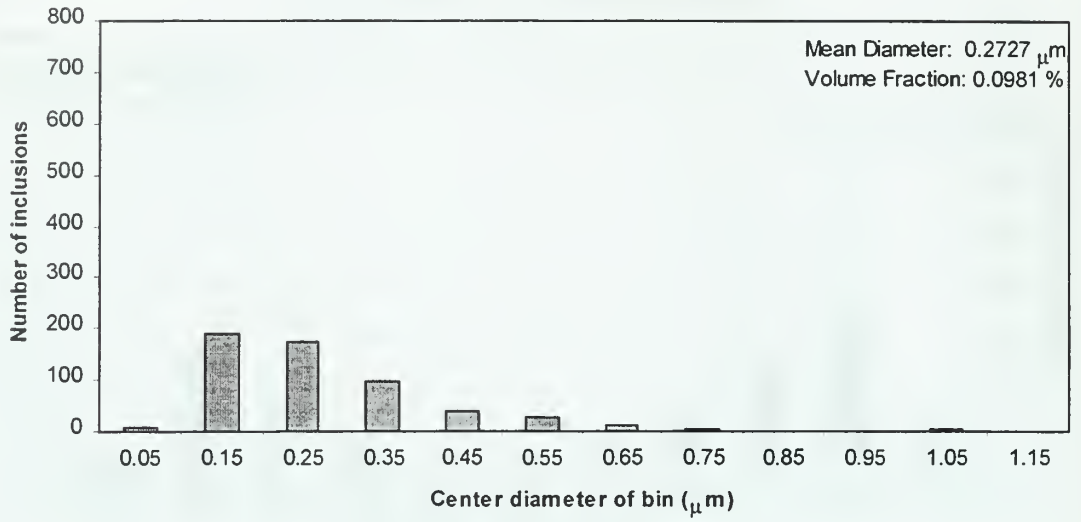

PD 21242 DIAMETER DISTRIBUTION

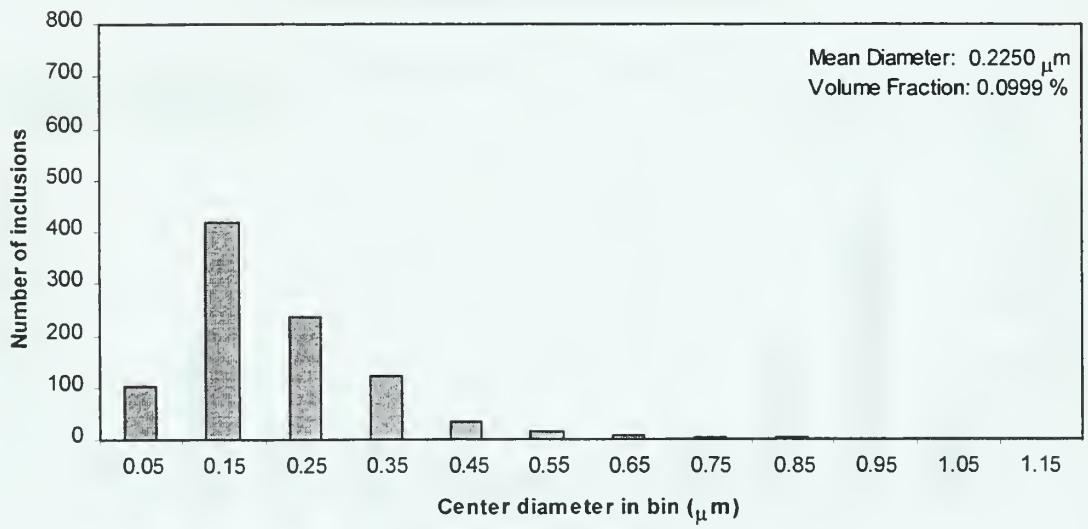

PD 21251 S2 DIAMETER DISTRIBUTION

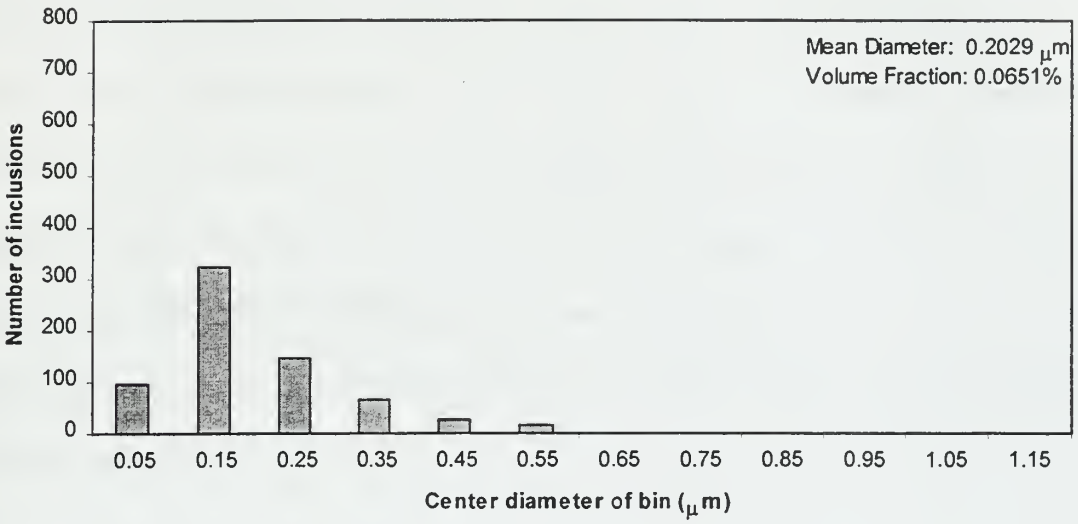

PD 21255 DIAMETER DISTRIBUTION

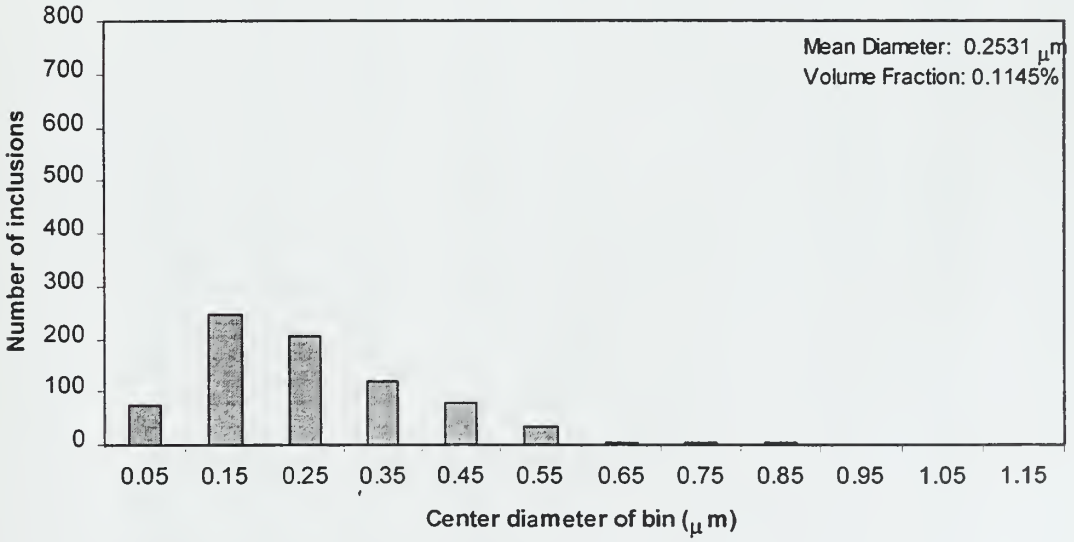

APPENDIX C. NON-METALLIC INCLUSION EDX CHEMISTRY

The following tables display the chemical information for the non-metallic inclusions that were analyzed using EDX analysis in the TEM. Some of the inclusions appeared to contain copper and sulfur as well as the elements in the table, but copper was not quantified because inaccurate readings would result from using copper grids. The sulfur was not quantified because mappings show that when sulfur is present, it is in the compound CuS. Since copper was not quantified, doing so to sulfur would not provide any useful results.

PD21092S1										
Inclusion	Oxygen		Aluminum		Silicon		Titanium		Manganese	
	wt%	at%	wt%	at%	wt%	at%	wt%	at%	wt%	at%
1	46.73	69.71	1.27	1.12	13.9	11.81	12.58	6.27	25.53	11.09
2	58.56	76.13	2.54	1.96	17.99	13.32	11.98	5.2	8.93	3.38
3	73.96	83.55	1.81	1.21	23.04	14.82	0.52	0.2	0.66	0.22
4	64.99	77.77	1.92	1.36	27.43	18.69	3.79	1.51	1.88	0.65
5	51.5	71.44	3.74	3.07	18.74	14.81	2.81	1.3	23.21	9.38
6	56.22	75.98	2.05	1.64	14.25	10.97	10.29	4.64	17.2	6.77
7	64.98	82.32	0.7	0.53	10.41	7.51	15.27	6.46	8.63	3.19
8	66.98	80.91	2.2	1.58	18.94	13.03	5.81	2.34	6.06	2.13
9	66.41	81.67	1.2	0.88	15.4	10.79	11.08	4.55	5.91	2.12
10	64.39	79.65	0.97	0.71	19.38	13.66	9.29	3.84	5.96	2.15
11	46.53	65.64	1.74	1.45	29.24	23.49	2.92	1.38	19.57	8.04
12	49.21	72.72	0.67	0.59	8.71	7.33	24.4	12.04	17	7.32
13	55.88	72.58	2.26	1.74	25.88	19.15	8.85	3.83	7.16	2.71
14	53.82	72.95	2.13	1.72	20.15	15.56	6.02	2.73	17.88	7.06
15	54.86	69.44	3.83	2.88	35.35	25.47	0.02	0.01	5.97	2.2
16	47.43	69.45	2.89	2.51	15.65	13.06	7.47	3.65	26.56	11.33
17	56.65	76.44	2.47	1.98	13.18	10.13	9.77	4.4	17.93	7.05
18	57.54	77.08	2.17	1.72	12.79	9.76	12.45	5.57	15.06	5.87
19	65.84	82.87	1.37	1.02	9.54	6.84	13.69	5.76	9.57	3.51
20	56.78	75.52	2.19	1.73	17.23	13.05	8.53	3.79	15.26	5.91
Avg.	**57.963**	**75.691**	**2.006**	**1.57**	**18.36**	**13.663**	**8.877**	**3.9735**	**12.797**	**5.104**
St. Dev.	**7.7275**	**5.1398**	**0.8606**	**0.6968**	**6.9538**	**4.9738**	**5.6896**	**2.7049**	**7.7237**	**3.3367**

PD21092S2										
Inclusion	Oxygen		Aluminum		Silicon		Titanium		Manganese	
	wt%	at%	wt%	At%	wt%	at%	wt%	at%	wt%	at%
1	56.28	71.97	2.75	2.08	29.18	21.25	5.54	2.37	6.25	2.33
2	55.83	72.28	2.46	1.89	27.09	19.98	6.05	2.62	8.57	3.23
3	55.98	72.17	2.6	1.99	27.99	20.55	4.5	1.94	8.93	3.35
4	48.7	66.78	3.56	2.89	29.33	22.91	1.13	0.52	17.28	6.62
5	61.26	76.4	2.6	1.93	23.61	16.77	6.61	2.75	5.91	2.15
6	57.78	72.74	3.24	2.42	29.15	20.9	6.05	2.55	3.78	1.39
7	49.68	68.81	2.53	2.08	24.64	19.44	5.57	2.58	17.58	7.09
8	53.12	68.34	3.31	2.53	35.22	25.81	3.62	1.56	4.73	1.77
9	53.95	72.82	2.64	2.12	20.22	15.55	6.66	3.15	16.2	6.37
10	50.07	69.34	1.36	1.12	25.55	20.15	1.68	0.78	21.35	8.61
11	61.6	74.24	2.7	1.93	33.4	22.93	1.78	0.72	0.51	0.18
12	53.31	71.14	2.74	2.17	25.42	19.32	2.88	1.28	15.65	6.08
13	49.17	68.78	2.12	1.75	24.31	19.37	2.61	1.22	21.8	8.88
14	46.18	65.16	1.65	1.38	30.43	24.46	1.15	0.54	20.6	8.46
15	42.86	59.34	3.43	2.82	41.76	32.93	1.53	0.71	10.4	4.19
16	55.68	72.91	3.05	2.37	23.92	17.84	4.63	2.03	12.72	4.85
17	61.68	74.34	2.9	2.07	32.97	22.63	1.92	0.77	0.54	0.19
18	56.23	75.71	1.68	1.35	16.27	12.48	5.94	2.67	19.87	7.79
19	52.34	70.19	11.87	9.44	16.39	12.52	4.85	2.17	14.56	5.68
20	61.02	74.95	2.87	2.09	28.58	20	5.14	2.11	2.39	0.86
Avg.	54.136	70.921	3.103	2.421	27.272	20.39	3.992	1.752	11.481	4.5035
St. Dev.	5.2701	4.0426	2.1442	1.7107	6.0813	4.5482	1.9734	0.8662	7.1857	2.9215

PD 21149										
Inclusion	Oxygen		Aluminum		Silicon		Titanium		Manganese	
	wt%	at%	wt%	At%	wt%	at%	wt%	at%	wt%	at%
1	3.3	10.02	1.75	3.15	3.5	6.04	0.52	0.52	90.93	80.27
2	60.48	73.49	1.14	0.82	35.35	24.46	3.01	1.22	0.02	0.01
3	61.08	75.94	1.48	1.09	26.92	19.07	1.6	0.67	8.91	3.23
4	48.85	68.27	2.88	2.39	24.32	19.36	3.86	1.8	20.1	8.18
5	50.92	69381	2.09	1.7	25.16	19.65	2.06	0.94	19.78	7.9
6	48.42	68.24	1.74	1.45	24.75	19.87	2.2	1.04	22.9	9.4
7	64.51	77.39	1.32	0.94	28.55	19.51	3.87	1.55	1.75	0.61
8	46.94	67.43	2.02	1.72	23.49	19.22	1.66	0.8	25.89	10.83
9	46.36	66.54	2.78	2.37	24.29	19.85	2.27	1.09	24.29	10.15
10	43.79	64.72	3.48	3.05	22.79	19.19	2.46	1.21	27.48	11.83
11	47.63	67.86	3	2.54	22.17	17.99	5.5	2.62	21.69	9
12	56.16	73.65	2.07	1.61	23.33	17.43	4.83	2.12	13.6	5.19
13	49.73	69.53	2.4	1.99	22.56	17.97	3.44	1.61	21.86	8.9
14	41.71	63.26	3.42	3.08	22.13	19.12	1.38	0.7	31.36	13.85
15	41.56	61.39	2.56	2.26	28.38	24.08	2.95	1.47	24.88	10.79
16	46.67	66.64	2.19	1.85	25.47	20.71	1.87	0.89	23.81	9.9
17	55.48	72.07	1.55	1.2	28.49	21.08	3.03	1.31	11.45	4.33
18	0.73	2.31	3.31	6.24	2.73	4.94	2.18	2.31	91.05	84.2
19	4.54	13.16	4.3	7.41	2.97	4.91	0	0	88.19	74.52
20	46.88	66.82	2.18	1.84	25.43	20.65	1.72	0.82	23.79	9.87
Avg.	43.287	3525.5	2.383	2.435	22.139	17.755	2.5205	1.2345	29.687	18.648
St. Dev.	18.521	15501	0.8279	1.66	8.7673	5.6462	1.3409	0.6385	27.268	26.586

PD 21150										
Inclusion	Oxygen		Aluminum		Silicon		Titanium		Manganese	
	wt%	at%	wt%	at%	wt%	at%	wt%	at%	wt%	at%
1	55	72.39	2.89	2.26	25.07	18.79	0.48	0.21	16.56	6.35
2	48.79	67.67	1.97	1.62	27.75	21.92	1.83	0.85	19.67	7.95
3	46.22	66.77	2.49	2.13	23.45	19.3	1.45	0.7	26.4	11.11
4	50.12	68.69	2.23	1.81	27.4	21.39	0.56	0.26	19.69	7.86
5	48.26	68.8	2.46	2.08	21.35	17.34	2.99	1.43	24.93	10.35
6	49.95	68.4	2.57	2.08	27.59	21.52	1	0.46	18.9	7.54
7	45	65.6	2.91	2.51	23.72	19.69	2.4	1.17	25.98	11.03
8	50.62	70.57	2.25	1.86	21.19	16.83	3.56	1.66	22.39	9.09
9	44.97	65.8	3.65	3.17	21.8	18.17	4.03	1.97	25.54	10.88
10	46.03	66.61	2.26	1.94	23.73	19.56	1.46	0.71	26.52	11.18
11	39.9	60.13	6.36	5.68	25.12	21.57	0.93	0.47	27.69	12.15
12	49.98	69.52	2.29	1.89	23.11	18.31	5.1	2.37	19.51	7.9
13	47.12	67.16	2.66	2.24	24.45	19.85	0.73	0.35	25.05	10.4
14	49.85	69.29	2.05	1.69	24.44	19.35	1.55	0.72	22.11	8.95
15	53.32	71.17	2.33	1.85	25.97	19.75	1.59	0.71	16.78	6.52
16	46.78	67.4	2.29	1.96	22.83	18.74	1.75	0.84	26.35	11.06
17	56.74	73.33	1.76	1.35	26.43	19.46	3.62	1.56	11.45	4.31
18	56.74	73.32	1.75	1.34	26.44	19.46	3.62	1.56	11.45	4.31
19	44.46	65.04	2.43	2.11	24.9	20.75	1.37	0.67	26.83	11.43
20	50.16	70.08	2.4	1.99	21.84	17.38	2.39	1.11	23.22	9.45
Avg.	49.001	68.387	2.6	2.178	24.429	19.457	2.1205	0.989	21.851	8.991
St. Dev.	4.2523	3.1215	0.9812	0.9148	2.0675	1.4539	1.298	0.5967	4.9625	2.3377

PD 21151										
Inclusion	Oxygen		Aluminum		Silicon		Titanium		Manganese	
	wt%	at%	wt%	at%	wt%	at%	wt%	at%	wt%	at%
1	43.64	64.67	1.9	1.67	24.34	20.54	1.92	0.95	28.2	12.17
2	41.55	63.9	1.85	1.68	20.48	17.94	4.52	2.32	31.61	14.16
3	41.94	63.98	1.82	1.65	21.6	18.77	3.32	1.69	31.32	13.92
4	40.58	63.26	1.38	1.28	20.2	17.94	5.16	2.69	32.68	14.84
5	45.28	67.09	1.46	1.28	20.32	17.15	4.23	2.09	28.72	12.39
6	40.62	63.02	1.28	1.18	21.42	18.93	4.62	2.39	32.06	14.48
7	42.98	64.94	2.03	1.82	20.8	17.9	4.51	2.28	29.67	13.06
8	24.23	47.59	2.48	2.88	13.29	14.86	4.1	2.69	55.91	31.97
9	13.02	31.07	2.05	2.9	9.77	13.28	4.79	3.82	70.38	48.93
10	40.1	62.37	1.89	1.74	21.52	19.07	4.28	2.22	32.22	14.6
11	41.96	63.94	1.65	1.49	22.08	19.16	2.7	1.37	31.61	14.03
12	43.37	65.28	1.71	1.52	21.08	18.07	4.54	2.28	29.3	12.84
13	37.7	59.76	1.73	1.63	23.82	21.51	2.17	1.15	34.57	15.96
14	51.57	68.49	2.15	1.69	31.65	23.94	3.9	1.73	10.74	4.15
15	45.82	65.55	1.62	1.38	27.47	22.38	3.96	1.89	21.12	8.8
16	38.71	60.99	1.57	1.47	22.64	20.32	3.09	1.63	33.98	15.59
17	42.16	63.84	1.86	1.67	22.49	19.4	4.98	2.52	28.52	12.58
18	38.57	61.11	1.29	1.22	21.83	19.7	4.48	2.37	33.82	15.6
19	38.56	61.03	1.67	1.57	22.18	19.99	1.21	0.64	36.39	16.77
20	34.67	56.68	1.87	1.81	24.48	22.8	2.02	1.1	36.97	17.6
Avg.	39.352	60.928	1.763	1.6765	21.673	19.183	3.725	1.991	33.49	16.222
St. Dev.	8.1182	8.2781	0.2958	0.4566	4.433	2.5062	1.1555	0.7376	11.876	9.2036

PD 21151S2										
Inclusion	Oxygen		Aluminum		Silicon		Titanium		Manganese	
	wt%	at%	wt%	at%	wt%	at%	wt%	at%	wt%	at%
1	47.03	67.96	1.01	0.87	22.8	18.77	2.25	1.09	26.91	11.32
2	46.85	68.12	1.03	0.89	21.53	17.83	3.45	1.67	27.14	11.49
3	48.49	68.88	1.19	1	23.32	18.87	1.18	0.56	25.82	10.68
4	45.75	67.38	1.01	0.88	21.56	18.09	1.08	0.53	30.59	13.12
5	49.89	68.11	1.33	1.08	29.85	23.21	1.38	0.63	17.54	6.97
6	45.58	66.47	0.9	0.78	24.36	20.23	2.14	1.04	27.01	11.47
7	46.83	68.08	1.2	1.03	21.61	17.89	2.25	1.09	28.12	11.9
8	47.83	68.42	1.08	0.92	23.3	18.98	1.56	0.75	26.23	10.93
9	41.5	63.53	1.22	1.11	22.78	19.86	1.72	0.88	32.78	14.62
10	48.18	68.93	1.04	0.88	22.43	18.28	1.59	0.76	26.76	11.15
11	46.75	68.11	1.02	0.89	21.4	17.76	2.6	1.26	28.22	11.98
12	42.2	63.94	1.26	1.13	23.38	20.18	1.7	0.86	31.47	13.89
13	39.77	61.19	1.24	1.13	25.93	22.72	2.23	1.15	30.83	13.81
14	42.88	64.82	1.05	0.95	22.32	19.22	2.53	1.28	31.22	13.74
15	44.22	65.68	1.08	0.96	22.98	19.45	3.12	1.55	28.59	12.37
16	41.98	64.24	1.31	1.19	21.71	18.92	0.96	0.49	34.04	15.17
17	47.14	68.49	1.32	1.14	20.81	17.23	2.27	1.1	28.46	12.04
18	30.2	51.22	1.62	1.63	27.53	26.6	6.68	3.78	33.97	16.78
19	25.43	44.97	1.53	1.6	31.84	32.08	1.75	1.04	39.45	20.32
20	36.78	58.93	0.65	0.62	25	22.82	1.55	0.83	36.01	16.8
Avg.	43.605	64.66	1.1811	1.0558	23.76	20.325	2.2337	1.1321	29.218	12.829
St. Dev.	6.2603	6.2765	0.2171	0.2423	2.9282	3.5951	1.2387	0.7033	4.5951	2.8294

PD 21176										
Inclusion	Oxygen		Aluminum		Silicon		Titanium		Manganese	
	wt%	at%	wt%	at%	wt%	at%	wt%	at%	wt%	at%
1	31.87	51.66	10.05	9.66	24.49	22.61	2.96	1.6	30.64	14.46
2	46.45	66.64	6.96	5.92	19.41	15.86	3.74	1.79	23.44	9.79
3	45.95	66.07	7.66	6.53	19.38	15.87	3.32	1.59	23.7	9.92
4	44.33	64.26	8.18	7.03	21.12	17.44	2.31	1.12	24.05	10.15
5	34.13	54.73	9.7	9.23	21.07	19.25	5.76	3.09	29.34	13.7
6	45.34	64.97	8.52	7.24	21.13	17.24	1.78	0.85	23.23	9.69
7	44.8	64.42	8.84	7.54	21.24	17.39	1.96	0.94	23.16	9.7
8	45.03	64.95	8.19	7	20.52	16.86	2.59	1.25	23.68	9.95
9	46.16	66.46	6.52	5.57	19.84	16.27	3.04	1.46	24.44	10.25
10	44.07	64.73	6.96	6.07	19.57	16.37	4.1	2.01	25.3	10.82
11	45.18	65.58	6.75	5.81	19.97	16.51	3.66	1.77	24.44	10.33
12	40.9	60.9	9.58	8.46	21.86	18.54	1.67	0.83	26	11.27
13	45.39	65.41	7.6	6.49	20.44	16.78	2.67	1.28	23.91	10.03
14	45.95	66.8	5.85	5.04	18.28	15.13	5.69	2.77	24.23	10.26
15	46.79	66.67	8.03	6.79	19.04	15.45	4.11	1.96	22.03	9.14
16	42.7	63.41	7.24	6.37	20.12	17.02	3.88	1.92	26.06	11.27
17	42.16	62.62	8.07	7.1	20.63	17.46	3.34	1.66	25.81	11.16
18	38.48	59.39	6.73	6.16	22.6	19.87	1.54	0.8	30.65	13.78
19	44.96	65.08	10.67	9.16	16.77	13.83	4.77	2.31	22.84	9.63
20	28.5	48.57	7.76	7.84	24.38	23.67	5.26	3	34.1	16.93
Avg.	42.457	62.666	7.993	7.0505	20.593	17.471	3.4075	1.7	25.553	11.112
St. Dev.	5.2126	5.2031	1.2738	1.2737	1.8336	2.3794	1.2859	0.6893	3.1733	2.0237

PD 21242										
Inclusion	Oxygen		Aluminum		Silicon		Titanium		Manganese	
	wt%	at%	wt%	at%	wt%	at%	wt%	at%	wt%	at%
1	46.04	66.63	3.01	2.58	22.77	18.77	2.24	1.08	25.94	10.93
2	46.76	67.94	1.05	0.9	21.71	17.97	4.76	2.31	25.71	10.88
3	54.8	72.64	1.52	1.19	24.11	18.21	7.05	3.12	12.52	4.83
4	61.37	74.17	2.3	1.65	33.5	23.06	2.55	1.03	0.29	0.1
5	54.5	73.15	1.25	1	22.2	16.97	4.63	2.08	17.41	6.8
6	35.56	60.12	1.67	1.67	13.07	12.59	15.75	8.9	33.95	16.72
7	50.41	69.12	2.17	1.76	26.04	20.34	4.03	1.85	17.35	6.93
8	57.55	72.88	2.13	1.6	29.89	21.55	2.26	0.96	8.17	3.01
9	54.99	72.38	2.09	1.63	25.47	19.1	3.59	1.58	13.85	5.31
10	55.47	72.01	2.17	1.67	27.97	20.69	3.36	1.46	11.02	4.17
11	58.05	73.4	1.66	1.24	29.46	21.22	2.78	1.17	8.05	2.97
12	53.64	72.03	1.61	1.28	23.71	18.13	5.69	2.55	15.35	6
13	46.81	67.92	1.24	1.06	21.89	18.1	3.47	1.68	26.59	11.24
14	62.33	76.22	1.68	1.22	27.73	19.31	5.87	2.4	2.39	0.85
15	71.95	83.38	0.94	0.64	20.43	13.48	4.91	1.9	1.77	0.6
16	67.09	80.23	1.68	1.19	22.14	15.08	6.46	2.58	2.64	0.92
17	63.03	75.9	1.46	1.04	31.05	21.3	3.81	1.53	0.64	0.22
18	62.97	76.14	1.48	1.06	29.92	20.61	4.07	1.64	1.56	0.55
19	48.62	68.08	2.07	1.72	25.3	20.17	3.98	1.86	20.04	8.17
20	46.51	67.59	0.76	0.65	22.92	18.97	2.71	1.32	27.1	11.47
Avg.	54.923	72.097	1.697	1.3375	25.064	18.781	4.6985	2.15	13.617	5.6335
St. Dev.	8.5865	5.1439	0.535	0.4542	4.6222	2.6687	2.9388	1.6907	10.466	4.7388

PD 21251S2										
Inclusion	Oxygen		Aluminum		Silicon		Titanium		Manganese	
	wt%	at%	wt%	at%	wt%	at%	wt%	at%	wt%	at%
1	53.56	74.4	4.25	3.5	10.75	8.5	14.73	6.84	16.72	6.76
2	51.07	73.17	3.41	2.9	10.14	8.28	14.69	7.03	20.68	8.63
3	54.16	75.88	3.98	3.3	6.58	5.25	19.47	9.11	15.82	6.46
4	50.11	72.29	3.47	2.97	10.8	8.87	14.61	7.04	21.02	8.83
5	51.62	73.6	3.32	2.81	9.92	8.06	15.51	7.38	19.63	8.15
6	50.78	72.05	4.29	3.61	12.57	10.16	13.45	6.37	18.91	7.81
7	49.14	71.75	4.25	3.68	9.14	7.6	16.44	8.02	21.03	8.94
8	51.51	73.95	3.69	3.14	7.86	6.43	16.75	8.03	20.2	8.44
9	36.77	60.1	4.18	4.05	14.15	13.18	18.44	10.07	26.46	12.6
10	50.91	72.73	3.87	3.28	10.75	8.74	14.74	7.03	19.73	8.21
11	53.13	73.35	3.86	3.16	13.66	10.74	16.18	7.46	13.17	5.29
12	47.08	70.71	3.65	3.25	7.94	6.79	18.09	9.08	23.24	10.17
13	2.05	6.17	3.11	5.53	4.07	6.96	15.3	15.34	75.47	66
14	46.79	71.26	3.04	2.74	4.69	4.07	26.92	13.7	18.57	8.23
15	53.76	75.77	3.02	2.53	7.15	5.74	19.26	9.07	16.81	6.9
16	9.14	23.48	6.02	9.17	5.26	7.7	1.29	1.11	78.28	58.54
17	49.73	73.11	3.32	2.9	6.35	5.31	20.48	10.06	20.12	8.62
18	52.26	74.46	3.79	3.21	7.35	5.96	19.55	9.3	17.05	7.07
19	50.87	74.23	2.98	2.58	5.55	4.61	21.25	10.36	19.35	8.22
20	51.06	73.08	4.54	3.85	8.54	6.96	18.95	9.06	16.9	7.05
Avg.	45.775	66.777	3.802	3.608	8.661	7.4955	16.805	8.573	24.958	13.546
St. Dev.	14.281	18.274	0.7033	1.4659	2.9077	2.2112	4.8094	2.8581	17.982	16.774

PD 21255										
Inclusion	Oxygen		Aluminum		Silicon		Titanium		Manganese	
	wt%	at%	wt%	at%	wt%	at%	wt%	at%	wt%	at%
1	56.09	69.94	0.57	0.42	39.55	28.09	3.27	1.36	0.52	0.19
2	57.37	72.16	0.88	0.66	33.05	23.68	5.89	2.47	2.81	1.03
3	55.89	70.52	0.52	0.39	36.39	26.16	5.38	2.27	1.82	0.67
4	60.29	75.12	0.49	0.36	28.6	20.3	6.91	2.88	3.71	1.35
5	52.78	67.42	0.47	0.36	40.98	29.81	4.8	2.05	0.96	0.36
6	55	70.39	2.04	1.55	32.74	23.87	7.13	3.05	3.09	1.15
7	57.18	74.83	0.55	0.43	21.59	16.1	13.75	6.01	6.92	2.64
8	59.22	73.76	0.21	0.16	31.9	22.63	5.87	2.44	2.8	1.02
9	56.67	70.29	0.56	0.41	39.66	28.02	2.79	1.16	0.32	0.11
10	59.88	73.24	0.1	0.07	36.05	25.12	3.07	1.25	0.91	0.32
11	58.26	72.83	0.38	0.28	33.09	23.56	5.8	2.42	2.48	0.9
12	55.72	69.25	0.18	0.13	42.1	29.8	1.8	0.75	0.21	0.07
13	56.04	70.73	0.53	0.39	35.93	25.83	5.43	2.29	2.08	0.77
14	58.66	73.87	1.41	1.05	28.63	20.54	7.25	3.05	4.05	1.48
15	53.73	70.5	1.13	0.88	29.66	22.16	9.72	4.26	5.76	2.2
16	54.31	72.34	1.33	1.05	24.58	18.65	5.13	2.28	14.65	5.68
17	60.34	74.82	1.08	0.79	29.33	20.71	6.23	2.58	3.02	1.09
18	58.94	74.1	0.96	0.71	28.87	20.67	7.47	3.14	3.76	1.38
19	58.23	72.75	0.58	0.43	33.21	23.63	5.25	2.19	2.73	0.99
20	81.87	88.76	2.78	1.78	15.26	9.42	0	0	0.1	0.03
Avg.	58.324	72.881	0.8375	0.615	32.059	22.938	5.647	2.395	3.135	1.1715
St. Dev.	5.9513	4.288	0.6601	0.4561	6.6596	4.8334	2.9092	1.273	3.2545	1.2622

INITIAL DISTRIBUTION LIST

No. Copies

1. Defense Technical Information Center
   8725 John J. Kingman Rd., STE 0944
   Ft. Belvoir, Virginia 22060-6218.....2

2. Dudley Knox Library
   Naval Postgraduate School
   411 Dyer Rd.
   Monterey, California 93943-5100.....2

3. Engineering and Technology Curricular Office, Code 34
   Naval Postgraduate School
   700 Dyer Rd., Bldg. 245
   Monterey, California 93943-5100.....1

4. Department Chairman, Code ME/Mc
   Department of Mechanical Engineering
   Naval Postgraduate School
   700 Dyer Rd., Bldg. 245
   Monterey, California 93943-5100.....1

5. Dr. Alan G. Fox, Code ME/Fx
   Department of Mechanical Engineering
   Naval Postgraduate School
   700 Dyer Rd., Bldg. 245
   Monterey, California 93943-5100.....2

6. Dr. Sarath Menon, Code ME/Ms
   Department of Mechanical Engineering
   Naval Postgraduate School
   700 Dyer Rd., Bldg. 245
   Monterey, California 93943-5100.....1

7. Mr. Joe Blackburn
   Naval Surface Warfare Center
   Carderock Division, Code 615
   9500 McArthur Boulevard
   Bethesda, Maryland 20084-5000.....1

8. Mr. R. DeNale
Naval Surface Warfare Center
Carderock Division, Code 615
9500 McArthur Boulevard
Bethesda, Maryland 20084-5000.....1

9. Jonathon J. Van Slyke
362A Shark Blvd.
Groton, CT 06340.....2